

Received 2018 March 22; revised 2018 June 29; accepted 2018 July 2

DRAFT VERSION AUGUST 7, 2018

Typeset using L^AT_EX **preprint2** style in AASTeX62

The Gas Composition and Deep Cloud Structure of Jupiter’s Great Red Spot

G. L. BJORAKER,¹ M. H. WONG,² I. DE PATER,² T. HEWAGAMA,³ M. ÁDÁMKOVICS,⁴ AND G. S. ORTON⁵

¹*NASA/GSFC Code 693, Greenbelt, MD 20771, USA*

²*Department of Astronomy, University of California, Berkeley, CA 94720-3411, USA*

³*University of Maryland, College Park MD 20742-4111, USA*

⁴*Department of Physics and Astronomy, Clemson University, Clemson, SC 29634-0978, USA*

⁵*Jet Propulsion Laboratory and California Institute of Technology, Pasadena, CA 91109, USA*

ABSTRACT

We have obtained high-resolution spectra of Jupiter’s Great Red Spot (GRS) between 4.6 and 5.4 μm using telescopes on Mauna Kea in order to derive gas abundances and to constrain its cloud structure between 0.5 and 5 bars. We used line profiles of deuterated methane (CH_3D) at 4.66 μm to infer the presence of an opaque cloud **at 5 ± 1 bars**. From thermochemical models this **is almost certainly** a water cloud. We also used the strength of Fraunhofer lines in the GRS to obtain the ratio of reflected sunlight to thermal emission. The level of the reflecting layer was constrained to be at **570 ± 30 mbars** based on fitting strong NH_3 lines at 5.32 μm . We identify this layer as an ammonia cloud based on the temperature where gaseous NH_3 condenses. We found evidence for a strongly absorbing, but not totally opaque, cloud layer at pressures deeper than 1.3 bars by combining Cassini/CIRS spectra of the GRS at 7.18 μm with ground-based spectra at 5 μm . This is consistent with the predicted level of an NH_4SH cloud. We also constrained the vertical profile of H_2O and NH_3 . The GRS spectrum is matched by a saturated H_2O profile above an opaque water cloud at 5 bars. The pressure of the water cloud constrains Jupiter’s O/H ratio to be at least 1.1 times solar. The NH_3 mole fraction is **200 ± 50 ppm** for pressures between 0.7 and 5 bars. Its abundance is **40 ppm** at the estimated pressure of the reflecting layer. We obtained **0.8 ± 0.2 ppm** for PH_3 , a factor of 2 higher than in the warm collar surrounding the GRS. We detected all 5 naturally occurring isotopes of germanium in GeH_4 in the Great Red Spot. We obtained an average value of **0.35 ± 0.05 ppb** for GeH_4 . Finally, we measured **0.8 ± 0.2 ppb** for CO in the deep atmosphere.

Keywords: planets and satellites: individual (Jupiter) — planets and satellites: atmospheres

1. INTRODUCTION

The Great Red Spot is a high-pressure region in the atmosphere of Jupiter, producing an anticy-

clonic storm 22° south of the planet’s equator. The spot is large enough to contain two or three planets the size of Earth. There have been numerous studies of various aspects of the Great Red Spot (GRS) including its wind field (Simon-Miller et al. (2002), Asay-Davis et al. (2009)), its mysteri-

ous red color (Loeffler et al. (2016), Carlson et al. (2016)), its significant shrinkage in size (Asay-Davis et al. (2009), Simon et al. (2014)) and its overall dynamics (e.g. Marcus (1993), Read et al. (2006), Palotai et al. (2014)).

There have also been numerous studies of the vertical cloud structure of the GRS. Banfield et al. (1998) used Galileo Solid State Imaging (SSI) data between 0.73 and 0.89 μm to infer a thick cloud over the GRS extending from 200 to 700 mbars. Irwin et al. (1999) reported a similar cloud structure for the GRS based on Baines et al. (1996). These authors used Galileo Near Infrared Mapping Spectrometer (NIMS) spectra of the GRS between 0.89 and 2.2 μm . This cloud forms at the level where NH_3 ice is expected to condense. However, Baines et al. (2002) found that spectrally identifiable ammonia clouds are present to the northwest of the GRS, but not in the spot itself. Clouds to the northwest were newly condensed and therefore fresh, while in the GRS cloud particles **may have evolved** through coating or compositional mixing (e.g. Atreya & Wong (2005); Kalogerakis et al. (2008); Sromovsky & Fry (2010)). Simon-Miller et al. (2001, 2002) used Galileo SSI data between 0.41 and 0.89 μm to infer the presence of an optically thin stratospheric haze, a moderate to dense tropospheric haze, and an optically thick, physically thin cloud sheet around 900 mbars.

Prior studies of gas composition in the GRS have mostly been limited to the upper levels of the feature, between about 100 - 500 mbar, due to opacity from aerosols and **Rayleigh** scattering. Retrievals of locally-depleted NH_3 in the 100 - 300 mbar range from Voyager IRIS (Griffith et al. 1992) and HST/FOS (Edgington et al. 1999) might seem to be at odds with locally-enhanced NH_3 abundance near the 500-mbar level from Cassini/CIRS (Achterberg et al. 2006). These results might be consistent if NH_3 decreases rapidly with height (0.5-km scale height), as found by Tokunaga et al. (1980) based on ground-based infrared spec-

troscopy. Fletcher et al. (2010) used multiple sources of thermal infrared data to show that there are also horizontal gradients of composition (as well as temperature and aerosol parameters) across the GRS. Fletcher et al. (2016) revisited the GRS using ground-based infrared spectral imaging with TEXES, confirming the north-south gradient of NH_3 concentration in the 500-mbar region. At radio frequencies, the Very Large Array (VLA) has been used to produce spectral maps of NH_3 concentrations at deeper levels on Jupiter, including the GRS (de Pater et al. 2016). Wavelengths from 1.7 - 5.5 cm probe the 0.6 - 6 bar pressure levels, where the GRS has higher NH_3 concentrations than most other regions of the planet (except for the Equatorial Zone and plumes of NH_3 -rich gas near 4°N). At these wavelengths, gaseous NH_3 is the principal opacity source, while cloud opacity is expected to be minimal.

In this paper we present ground-based observations of Jupiter's Great Red Spot between 4.6 and 5.4 μm . The 5- μm region is a window to the deep atmosphere of Jupiter because of a minimum in opacity due to H_2 and CH_4 . This spectrum provides a wealth of information about the gas composition and cloud structure of the troposphere. Jupiter's 5- μm spectrum is a mixture of scattered sunlight and thermal emission that varies significantly between Hot Spots and low-flux regions such as the Great Red Spot. Chemical models of Jupiter's cloud structure predict three distinct layers: an NH_3 ice cloud near **0.8 bars**, an NH_4SH cloud formed from a reaction of NH_3 and H_2S at **2.3 bars**, and a massive water ice/liquid solution cloud near **6 bars**, depending on assumptions of composition and thermal structure (see Weidenschilling & Lewis (1973), Atreya & Romani (1985), and Wong et al. (2015)). Thermal emission from the deep atmosphere is attenuated by the variable opacity at 5 μm of one or more of these three cloud layers.

The Great Red Spot has very low flux at 5 μm compared with adjacent regions. Previous 5-

μm datasets such as Voyager IRIS, Galileo NIMS, and spectra from the Kuiper Airborne Observatory of Jupiter provided a wealth of information on Hot Spots (e.g. Bjoraker et al. (1986a,b) and Roos-Serote et al. (2004)) but they did not have the combination of sensitivity, high spectral resolution, and spatial resolution required to model the Great Red Spot. In this study, the use of high resolution instrumentation on the Infrared Telescope Facility (IRTF) and Keck telescopes in Hawaii allows us for the first time to characterize the cloud structure and gas composition of the Great Red Spot at pressures between 0.5 and 5 bars.

The abundance of H_2O in Jupiter’s atmosphere is of fundamental importance in understanding the origin of Jupiter, the composition of its clouds, and jovian dynamics at pressures greater than 2 bars. One of the key objectives of the Juno mission, which began orbiting Jupiter in July 2016, is to measure water vapor below Jupiter’s clouds to determine the O/H ratio using the Microwave Radiometer (MWR) (Janssen et al. 2005). Interpretation of these data may not be straightforward, however, due to the small microwave absorptivity of H_2O gas compared with NH_3 (see de Pater et al. (2005) for details). Ground-based measurements of H_2O and NH_3 are important in order to provide upper boundary conditions to these key absorbers. Well-constrained values for these gases between 0.5 and 5 bars should improve the accuracy of the MWR’s measurements of H_2O and NH_3 down to 100 bars, which only Juno can perform.

In Fig. 1 we illustrate the complementarity of microwave and $5\text{-}\mu\text{m}$ spectra of Jupiter to probe the deep atmosphere. On the left, we show contribution functions **between $4.66\text{ }\mu\text{m}$ and $5.32\text{ }\mu\text{m}$** due to gas opacity alone. The strongest absorption lines sound near 1 bar, while weak features can probe down to **6 or 7 bars**. Three clouds are shown at their predicted levels from thermochemical models (e.g. Wong et al. (2015)). On the right we illustrate weighting functions for each of the six channels of the Microwave Radiometer, adapted from

Janssen et al. (2005). There is excellent overlap in sounding Jupiter between $5\text{ }\mu\text{m}$ and 3 of the 6 MWR channels, namely at 3.125 cm, 6.25 cm, and 12.5 cm. Early Juno results on measurements of NH_3 in the deep atmosphere using MWR were presented by Li et al. (2017b) and Ingersoll et al. (2017). In July, 2017 Juno’s orbit passed over the Great Red Spot yielding both spectacular images and microwave observations, which are currently being analyzed (Li et al. 2017a).

In the next section we describe the instrumentation, observing circumstances, and data selection for the Great Red Spot. In Section 3 we present spectra of Jupiter’s Great Red Spot from ground-based and Cassini data. We demonstrate that we can constrain the lower cloud structure of the GRS even when higher-altitude clouds greatly attenuate the thermal flux from the deep atmosphere. Bjoraker et al. (2015) modeled a Hot Spot in the South Equatorial Belt and a cloudy region in the South Tropical Zone. In the current study we apply the same methodology to constrain the pressure of the deepest clouds in Jupiter’s Great Red Spot. In addition, we model ground-based spectra at $5.3\text{ }\mu\text{m}$ and Cassini spectra at $7.2\text{ }\mu\text{m}$ to constrain the location of upper and mid-level clouds in the GRS. Using a 3-layer highly-simplified cloud model we derive the abundance of H_2O , NH_3 , PH_3 , GeH_4 , and CO in the deep atmosphere of the Great Red Spot. These abundances will help to understand the dynamics of the atmosphere in this unique feature on Jupiter.

2. OBSERVATIONS

Five-micron spectra of Jupiter were acquired using two instruments: iSHELL on NASA’s Infrared Telescope Facility (IRTF) and NIRSPEC on the Keck 2 telescope. iSHELL is a new echelle spectrometer with 16 orders dispersed onto a Teledyne 2048x2048 Hawaii 2RG HgCdTe array covering $4.52\text{-}5.24\text{ }\mu\text{m}$ using the M1 grating setting (Rayner et al. 2016). A $0.75'' \times 15''$ slit was aligned east-west on Jupiter at the latitude of the Great Red Spot, resulting in spectra with a resolv-

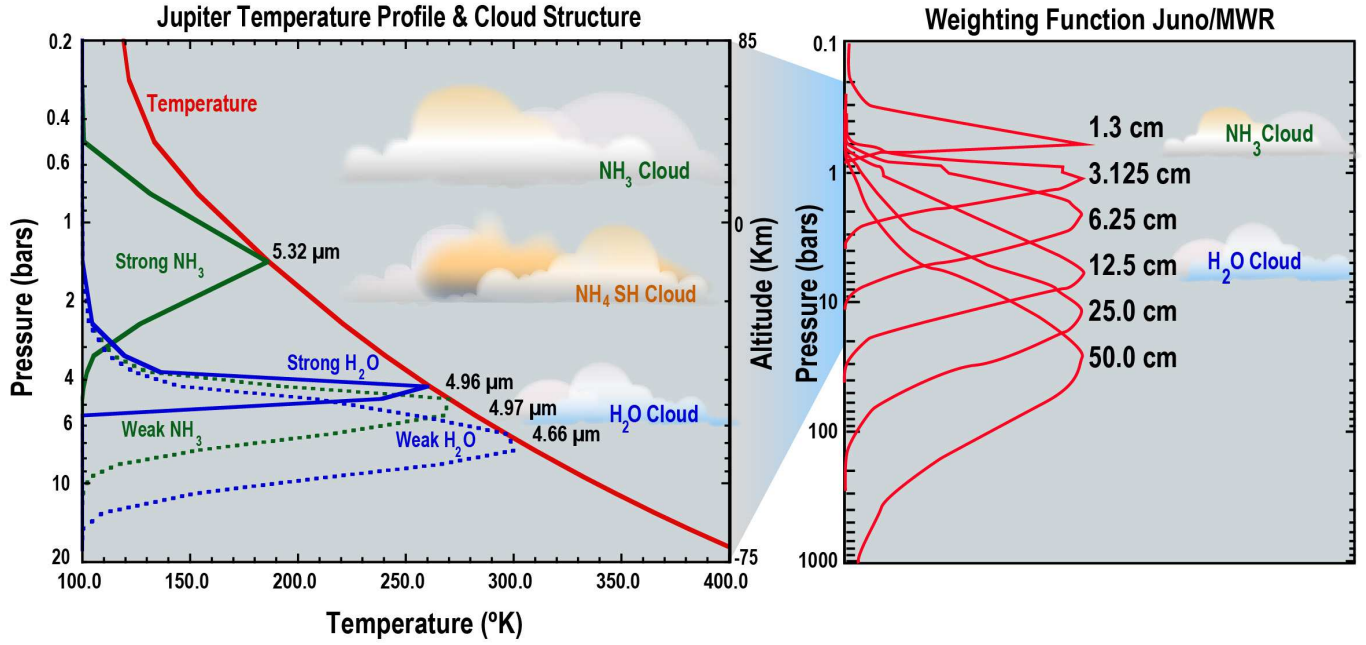


Figure 1. Contribution functions of Jupiter between $4.66 \mu\text{m}$ and $5.32 \mu\text{m}$ compared with MWR channels on Juno (Janssen et al. 2017). On the left, the Galileo probe temperature/pressure profile (Seiff et al. 1998) is shown in red for comparison.

ing power of 35,000. We analyzed 3 orders centered on 4.66 , 4.97 , and $5.16 \mu\text{m}$ in order to retrieve cloud structure, H₂O, and NH₃ in the Great Red Spot. The iSHELL spectra were obtained on May 18, 2017. Jupiter subtended $42''$ and the geocentric Doppler shift of the center of Jupiter was 18 km/sec. By selecting a time when the GRS was near the receding limb (planeto east or sky west) the resulting GRS spectrum had a Doppler shift of 28 km/sec due to Jupiter's rapid rotation. The water vapor column above Mauna Kea was 0.68 precipitable mm derived from fitting telluric lines in both stellar and Jupiter spectra. The seeing was 0.36 arcsec.

The combination of excellent seeing and low water vapor resulted in high quality spectra of Jupiter. Fig. 2 shows an image of Jupiter at $5.1 \mu\text{m}$ using the slit-viewing guide camera on iSHELL. The Great Red Spot appears dark at $5 \mu\text{m}$ due to thick clouds. There is a warm collar surrounding the GRS where clouds are much thinner. We analyzed a portion of the collar located $3.3''$ west of

the GRS. The image shows a slit that is $25''$ long. However, only a $15''$ subset of the slit (denoted by vertical bars) can be used at $5 \mu\text{m}$. Off-Jupiter spatial pixels were used to ensure proper sky subtraction. Fig. 3 is a composite image of the Great Red Spot taken with iSHELL using both the $5.1 \mu\text{m}$ filter and a K-band filter at $2.2 \mu\text{m}$ (blue). The Great Red Spot appears bright at $2.2 \mu\text{m}$ due to the presence of hazes in Jupiter's upper troposphere. Reflected light from deeper clouds outside of the GRS is attenuated by CH₄ and H₂ absorption. Note that excellent seeing reveals fine structure in the GRS and adjacent regions. Good seeing is also important to ensure that spectra of the GRS are not contaminated by $5 \mu\text{m}$ flux from adjacent regions.

NIRSPEC is an echelle spectrograph with 3 orders dispersed onto a 1024×1024 InSb array at our selected grating/cross-disperser settings of 60.48 / 36.9 (McLean et al. 1998). A $0.4'' \times 24''$ slit was aligned east-west on Jupiter at the latitude of the Great Red Spot, resulting in spectra with a resolv-

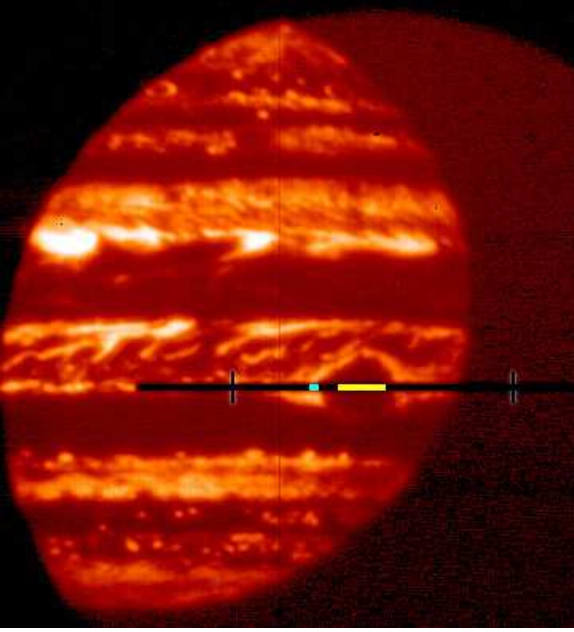


Figure 2. Image of Jupiter and the GRS at $5.1 \mu\text{m}$ using the slit-viewing camera on iSHELL. The GRS is dark due to thick clouds that block thermal radiation. Yellow pixels denote the portion of the Great Red Spot used in this analysis. Cyan pixels show the location of the Warm Collar spectrum west of the GRS.

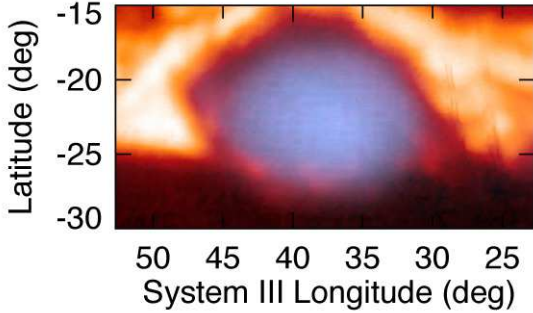


Figure 3. Composite map of GRS at $2.2 \mu\text{m}$ (blue) and at $5.1 \mu\text{m}$ using the slit-viewing camera on iSHELL. The seeing was 0.36 arcsec. The GRS is bright in methane-band images due to upper tropospheric haze around 200 mbars.

ing power of 20,000. We analyzed all 3 orders centered on 4.66, 4.97, and $5.32 \mu\text{m}$. The first two orders yielded spectra similar to that of iSHELL. The $5.32\text{-}\mu\text{m}$ order samples a strong NH_3 absorption band permitting retrieval of the pressure of the upper cloud layer. The NIRSPEC spectra were obtained on January 21, 2013. Jupiter subtended $44''$ and the geocentric Doppler shift of the GRS was 14.3 km/sec. The water vapor column

above Mauna Kea was 1.0 precipitable mm, derived from fitting telluric lines in both stellar and Jupiter spectra.

The third dataset used in this study was a selection of thermal infrared spectra acquired during the Cassini flyby of Jupiter from December 2000 to January 2001. CIRS was the Composite Infrared Spectrometer (Flasar et al. 2004), operating between 6.7 and $1000 \mu\text{m}$. We used mid-IR spectra of the Great Red Spot and of Hot Spots in the North Equatorial Belt covering wavelengths between 6.7 and $9.5 \mu\text{m}$ (1050 to 1495 cm^{-1}). The spectral resolution was 3.0 cm^{-1} . We averaged 22 of the hottest CIRS spectra in the NEB acquired at the highest spatial resolution (2.4° of latitude) on December 31, 2000. Next, we averaged 23 of the coldest spectra of the GRS ranging between 17°S and 23°S and 41 to 61° System III longitude with an average spatial resolution of 3° . We include these spectra to distinguish between cloud opacity in the NH_3 and NH_4SH layers, as described in Section 3.1.3.

In Fig. 4 we present context images of the Great Red Spot for each of the three spectroscopic datasets used in this study. The three columns correspond to the times of the Cassini flyby of Jupiter, of the Keck/NIRSPEC observations, and of the IRTF/iSHELL data, respectively. Each row sounds a different range of altitudes. Hazes in the upper troposphere near 200 mbars are bright at $0.89 \mu\text{m}$ and at $2.2 \mu\text{m}$ and dark in the ultraviolet. Chromophores mixed into the haze absorb strongly in both ultraviolet and blue wavelengths giving the GRS its red color (see Wong et al. (2011); Loeffler et al. (2016)). Ammonia and ammonium hydrosulfide clouds can be probed by reflected sunlight using filters in the optical and near-infrared. Finally, multiple cloud layers can be studied using thermal emission at $5 \mu\text{m}$ that originates between 5 and 10 bars and is attenuated by H_2O , NH_4SH , and NH_3 cloud opacity.

3. DATA ANALYSIS AND RESULTS

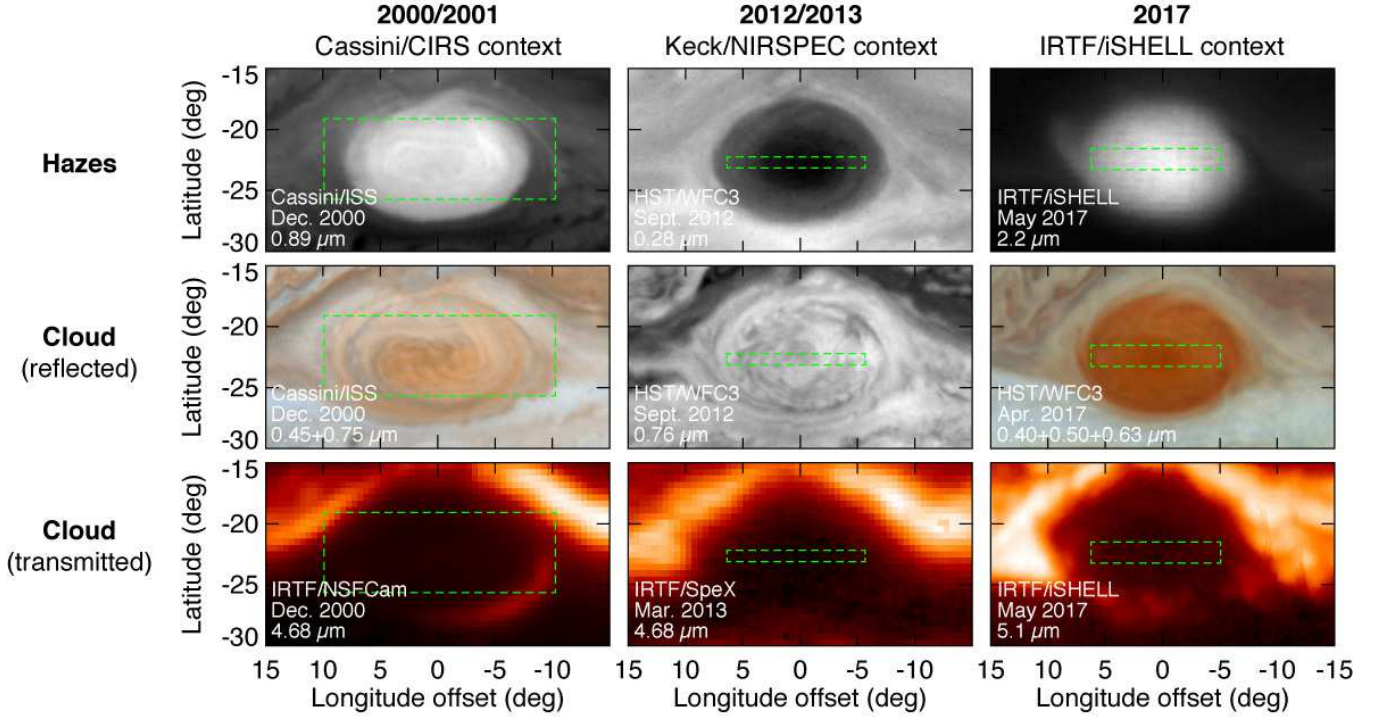


Figure 4. Context maps for GRS spectroscopic data. Each column corresponds to a different epoch, and each row senses different vertical layers. Green rectangles outline approximate areas used for spectral selection. Top row: Upper tropospheric hazes are isolated by strong CH_4/H_2 absorption or by Rayleigh scattering in the UV. Haze/chromophore boundaries have been shown to closely match the dynamical boundary of the vortex (de Pater et al. 2010; Wong et al. 2011). Our spectral footprints are within these boundaries. The CIRS spectral footprint (left column) appears in this figure to extend beyond the dynamical boundary of the vortex, but only the coldest spectra within this footprint were selected. In the UV (middle column), the haze within the GRS has a low single-scattering albedo, causing its central region to appear darker than the surroundings. Middle row: Overall cloud opacity in the NH_3 and NH_4SH layers modulates optical reflectivity. Bottom row: M-band brightness is shown on a log scale (top/middle rows are linear scale). Here, bright regions suggest low cloud opacity in both NH_3 and NH_4SH layers. Maps are shown for relative context and are not radiometrically calibrated. Sources: Cassini/ISS maps were obtained from <http://ciclops.org>. HST images in 2012 are from program GO-13067 (Karalidi et al. 2013), and the HST composite image from 2017 is from the OPAL program GO-14756 (Simon et al. 2015). IRTF maps from 2000 and 2013 are from co-author Orton. iSHELL maps for 2017 were obtained as guider images during our spectroscopic observations.

3.1. Cloud Structure

We present in this section a cloud model for the Great Red Spot that for the first time extends down to 5 bars on Jupiter. Studies of the GRS in the optical and in the mid-infrared are sensitive only to clouds at pressures less than 1 bar (presumably ammonia ice) and microwave measurements are not sensitive to clouds at all (unless they contain centimeter-size particles). The $5\text{-}\mu\text{m}$ window is the only spectral region that is sensitive to the levels of all 3 clouds (NH_3 , NH_4SH , and H_2O) predicted from thermochemical models. In order to simplify

the radiative transfer calculations, we made several approximations. The lower cloud was assumed to be semi-infinite, the upper clouds were modeled as purely absorbing, rather than as scattering layers, and each cloud layer was taken to be vertically thin (particle scale height much less than the gas scale height).

Our treatment of clouds as non-scattering absorbing/emitting layers may result in errors in the estimated transmittances of the cloud layers. Due to the strong dependence of the Planck function on temperature, the neglected

scattering component should be dominated by radiation from below each cloud layer (rather than back-scattered radiation from above the clouds). Microphysical upper limits to the radius of NH_3 and NH_4SH cloud particles are roughly 10 to 30 μm (Carlson et al. 1988); therefore, the scattering size parameter x of cloud particles ($x = 2\pi r/\lambda$) should be less than 40 at 4.6 μm , placing these particles in the Mie scattering regime in the absence of strong shape effects (Mishchenko & Travis 1998). The Mie single-scattering phase function is dominated by forward scattering, so both phase function and thermal profile arguments suggest that our scattering-free treatment is likely to lead to somewhat overestimated cloud transmittances. The dominance of upward-scattered emission over back-scattered emission in the spectrum means that our modeled gas abundances are not strongly affected by treatment of cloud layers. Gas abundances are derived from line shapes, and these should be preserved in the scattering process, if the scattered component is dominated by upwelling radiation. We now discuss each of the three clouds, beginning with the deepest one.

3.1.1. Lower cloud level

In the absence of clouds, the spectrum of Jupiter at 5 μm is formed between 1 and 10 bars, as shown in Fig. 1. Weak absorption lines near 4.67 μm (2142 cm^{-1}) sound levels deeper than 4 bars where temperatures are greater than 250 K. When cloud opacity is introduced to our model, the effect upon the spectrum depends on the temperature at the cloud level. Cold clouds, with temperatures less than 200 K, have the effect of attenuating the continuum without changing line to continuum ratios of weak absorption lines. This is because the radiance of a 250 K black body is 22 times that of a 200 K black body at 2142 cm^{-1} . A purely absorbing cloud of unit optical depth at 200 K will have the effect of multiplying the transmittance of a gas-only warm model atmosphere by

0.37. Self emission from the cold cloud is negligible at 2142 cm^{-1} . Warm clouds with temperatures greater than 250 K, on the other hand, will have significant self emission. This will affect the strength and shape of absorption lines in this spectral region. Thus, the continuum level is sensitive to the total cloud opacity in Jupiter’s atmosphere while spectral line shapes are sensitive only to the deepest (warmest) clouds. In this section we investigate the effect of the lower clouds on spectral line shapes. We match the observed continuum by multiplying the calculated spectrum by a constant factor to simulate purely absorbing upper (NH_3) and mid-level (NH_4SH) clouds.

The 4.7- μm spectrum of the GRS contains absorption lines of deuterated methane (CH_3D), phosphine (PH_3), and H_2O in Jupiter’s troposphere as well as Fraunhofer lines due to CO in the Sun. Jupiter is too warm for methane and its isotopologues to condense. Photochemical destruction of CH_4 occurs at pressures less than 1 mbar in Jupiter’s stratosphere, but not in the troposphere (Moses et al. 2005). We therefore assume that CH_4 and CH_3D have a constant mixing ratio with respect to H_2 in Jupiter’s troposphere. In that case variations in the strength and shape of CH_3D lines between the GRS and Hot Spots on Jupiter are due only to changes in cloud structure, not gas concentration as described in Bjoraker et al. (2015).

Fig. 5 shows iSHELL spectra at 4.66 μm (2144 cm^{-1}) of the Great Red Spot and of the Warm Collar at the same latitude 3.3'' to the west of the GRS. Due to excellent seeing, there is no contamination of the GRS spectrum from this or other warm regions. We performed an additional check for flux contamination by comparing the spectrum of the center 3 pixels (0.5'') of the GRS with the average of 15 pixels (2.5'') shown in Fig. 5. The spectra are nearly identical, but the signal-to-noise is better in the larger average. Note that CH_3D lines are much broader in the Warm Collar than in the GRS. **The radiance of the Warm Collar spectrum (right axis) is 13 times that of the GRS (left axis) at**

2142 cm^{-1} . The CH_3D lines are spectrally resolved at the iSHELL resolving power of 35,000 (0.06 cm^{-1} resolution). This is because molecules such as CH_3D typically have broadening coefficients of $0.06\text{ cm}^{-1}/\text{atm}$ and the line formation region on Jupiter at $4.66\text{ }\mu\text{m}$ takes place at pressures greater than 2 bars. In addition to CH_3D , this portion of the spectrum includes numerous Fraunhofer lines (denoted by S for solar). These lines are observed only in low-flux zone regions such as the GRS and not in Hot Spots. They provide evidence for a reflected solar component to the GRS spectrum at $5\text{ }\mu\text{m}$. Spectra of the Warm Collar and of Hot Spots, on the other hand, are dominated by thermal emission.

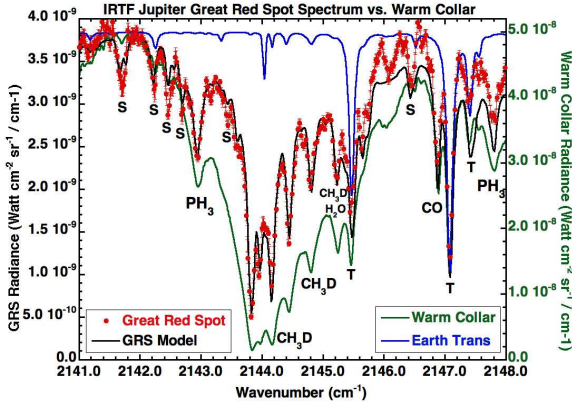


Figure 5. Comparison between IRTF / iSHELL spectra of the Great Red Spot (left axis) and of the Warm Collar (right axis) at $4.66\text{ }\mu\text{m}$. The Warm Collar is 13 times brighter than the GRS. Also shown is the best fitting model of the GRS and a model of the transmittance of the atmosphere above Mauna Kea. Transmittance scale (not shown) is 0 to 1.04. Telluric lines are denoted by T and solar lines by S.

Noise at $5\text{ }\mu\text{m}$ is primarily due to thermal emission of the relatively warm telescope and atmosphere above Mauna Kea, rather than detector noise or source noise. In a 5-second integration, there were 8000 counts on the sky (in strong water lines) and only 100 sky-subtracted counts on the GRS. We calculated the noise in the iSHELL spectrum of the Great Red Spot in two different ways. First, we measured the standard deviation of 70 spectral points near

2141 cm^{-1} in a spatial pixel that was well off of the limb of Jupiter. Next, we measured the standard deviation of the 15 spatial pixels that were used to create an average GRS spectrum, also near the continuum frequency at 2141 cm^{-1} . We divided by the square root of 15 to determine the standard error of the mean at each frequency. The first technique resulted in a signal to noise ratio (S/N) of 51 on the continuum. The second approach yielded $S/N = 53$. In Fig. 5 we show error bars for each spectral frequency using the second technique.

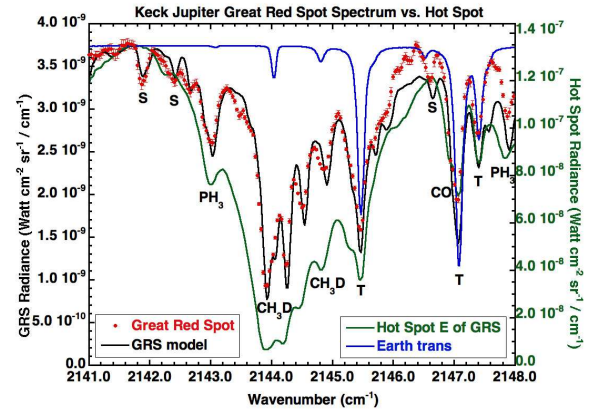


Figure 6. Comparison between Keck / NIRSPEC spectra of the Great Red Spot (left axis) and of a Hot Spot (right axis) at $4.66\text{ }\mu\text{m}$. The Hot Spot is 36 times brighter than the GRS. The NIRSPEC spectrum of the GRS is nearly identical to that obtained by iSHELL. The same radiative transfer model fits both Keck and IRTF spectra of the GRS. It was only necessary to change the spectral resolution, Doppler shift, and telluric water abundance to match each dataset.

Fig. 6 shows a very similar GRS spectrum acquired using NIRSPEC on the Keck telescope in 2013. Here we used the center 15 pixels ($2.9''$) of the GRS. The similarity of the GRS spectra using two different instruments 4 years apart shows the reproducibility of the data. Also shown is the spectrum of a Hot Spot $12.7''$ east of the GRS. As was the case with the Warm Collar, the CH_3D lines are much broader in the Hot Spot than in the GRS. The radiance of the Hot Spot spectrum (right axis) is 36 times that of the GRS (left axis) at 2141.7 cm^{-1} . Again, we are con-

ident that scattered light from adjacent regions is not getting into the GRS spectrum due to good seeing ($1.0''$) and due to the sheer size of the GRS (see Fig. 4). **A comparison between Fig. 5 and Fig. 6 reveals more Fraunhofer lines (marked s) in the iSHELL spectrum of the GRS. These particular Fraunhofer lines are not spectrally resolved at iSHELL resolution. The factor of 2 increased resolution of iSHELL with respect to NIRSPEC makes these lines much easier to detect on Jupiter. Higher spectral resolution also helps to separate jovian CO from telluric lines and to spectrally resolve the CH_3D lines in the GRS.**

We applied the same approach as before to determine the noise in the NIRSPEC spectrum of the GRS. We obtained a continuum S/N of 66 using off-Jupiter pixels and 80 using the variation between the 15 spatial pixels comprising the GRS spectrum. In Fig. 6 we show error bars for each spectral frequency using the second technique.

Absolute flux calibration was performed by smoothing the NIRSPEC spectrum of an NEB Hot Spot to 4.3 cm^{-1} resolution, dividing by the transmittance of the Earth's atmosphere above Mauna Kea, and scaling the radiance of the resulting spectrum to an average of Jupiter's NEB Hot Spots observed by Voyager IRIS in 1979. We performed a general validation of this Voyager-scaling calibration method by checking it against a Mars-based calibration. On March 25, 2014 we observed an SEB Hot Spot as well as Mars at $4.66\text{ }\mu\text{m}$ using the predecessor to iSHELL (CSHELL). **The Mars Climate Database (MCD) is a database of meteorological fields derived from General Circulation Model (GCM) numerical simulations of the Martian atmosphere (Millour et al. 2015). This database can be used to calculate the surface temperature of Mars at any season. We used the web interface to MCD ([http : //www - mars.lmd.jussieu.fr/mcd - python/](http://www-mars.lmd.jussieu.fr/mcd-python/)) to determine that the surface temperature near the**

sub-solar point on Mars was 279 K at the time. Using a 279-K black body for Mars, we determined that the continuum of the SEB Hot Spot at 2142 cm^{-1} corresponded to a brightness temperature of 271.3 K. We found that the Mars calibration and our Voyager-scaling method agreed to within 10%. The iSHELL spectrum of the GRS was normalized at 2142 cm^{-1} to the same radiance as in the NIRSPEC GRS spectrum.

There are numerous Fraunhofer lines visible in GRS spectra shown in Figures 5 and 6. We compared the equivalent width of the strongest line at 2141.8 cm^{-1} with its measured value in the Sun using ATMOS data (Farmer & Norton 1989; Farmer 1994). This line is 60% as strong as in the Sun; thus, 40% of the flux consists of thermal emission originating in the deep atmosphere that has been attenuated by one or more cloud layers before escaping to space. By multiplying the radiance of the continuum of the GRS at 2142 cm^{-1} by 0.6, we obtain the value of reflected radiance from upper clouds. The albedo of the GRS can be calculated by scaling the solar flux measured at Earth to 5.07 AU (Jupiter's heliocentric distance at the time of the NIRSPEC data). The reflected radiance is proportional to the cloud albedo and inversely proportional to the square of Jupiter's heliocentric distance. The result is that the albedo of the reflecting layer over the GRS is 17% at $4.66\text{ }\mu\text{m}$.

Synthetic spectra were calculated using the Spectrum Synthesis Program (SSP) line-by-line radiative transfer code as described in Kunde & Maguire (1974). The input temperature profile was obtained from the Galileo Probe (Seiff et al. 1998). Line parameters for CH_3D and other $5\text{-}\mu\text{m}$ absorbers are from GEISA 2003 (Jacquinet-Husson et al. 2005). Parameters for $\text{CH}_3\text{D-H}_2$ and $\text{CH}_3\text{D-He}$ broadening have been measured in the lab (Boussin et al. 1999; Lerot et al. 2003; Féjard et al. 2003). We used a broadening coefficient of $0.0613\text{ cm}^{-1}/\text{atm} (296/T)^{0.5}$ for CH_3D colliding with a mixture of 86.3% H_2 and 13.6% helium, as measured by the Galileo Probe (von Zahn et al.

1998). Pressure-induced H_2 coefficients were obtained using laboratory measurements at $5\ \mu\text{m}$ by Bachet et al. (1983) and the formalism developed by Birnbaum & Cohen (1976).

We investigated the effect of opaque lower clouds at 2, 5 and 7 bars on the $4.66\text{-}\mu\text{m}$ spectrum of the Great Red Spot. These levels correspond to opaque NH_4SH clouds and to opaque H_2O clouds at two different levels. **Synthetic spectra were calculated for a gas composition of 0.18 ppm CH_3D (Bjoraker et al. 2015; Lellouch et al. 2001)** and a saturated profile of H_2O above each lower cloud. The mole fraction of PH_3 was iterated to a value of 0.8 ppm to match the absorption feature at $2143\ \text{cm}^{-1}$, as described in Section 3.2.3.

The calculated GRS spectrum was split into two parts. The thermal component was convolved to $0.02\ \text{cm}^{-1}$ and Doppler-shifted by 28 and $14.3\ \text{km/sec}$ for iSHELL and NIRSPEC data, respectively. The reflected solar component was calculated using the same model but using only transmittances above a reflecting layer at 570 mbar (see next section) and for an albedo of 17% (as described above). The reflected component was convolved and Doppler-shifted. It was then multiplied by the ATMOS solar spectrum smoothed to $0.02\ \text{cm}^{-1}$ resolution. The thermal component was multiplied by transmittances of 0.4, 0.0185, and 0.0134 for models with an opaque cloud at 2, 5, and 7 bars, respectively, and added to the reflected spectrum. These values represent the transmission of cold, upper clouds. This, in turn, was multiplied by the transmission of the Earth's atmosphere above Mauna Kea at the time of the iSHELL or NIRSPEC data and finally smoothed to $0.06\ \text{cm}^{-1}$ resolution to match iSHELL or $0.10\ \text{cm}^{-1}$ to fit NIRSPEC spectra.

In Figures 7 and 8 we illustrate that the model with an opaque NH_4SH cloud at 2 bars (gold curve) does not fit the observed spectrum. In contrast, all CH_3D features, including the wing between 2143.2 and $2143.7\ \text{cm}^{-1}$ are equally well

matched by models with opaque clouds at 5 and 7 bars. The model with a deep cloud at 7 bars fits portions of the spectrum but the model with an opaque cloud at 5 bars (black curve) provides a better fit to the spectrum near $2138\ \text{cm}^{-1}$, as shown in Fig. 8. **We conclude that there must be significant cloud opacity at 5 ± 1 bars in the GRS. Based on the temperatures in this pressure range (257-290 K), thermochemical models rule out compositions of NH_3 or NH_4SH , so this cloud must consist of water in the ice or liquid phase.**

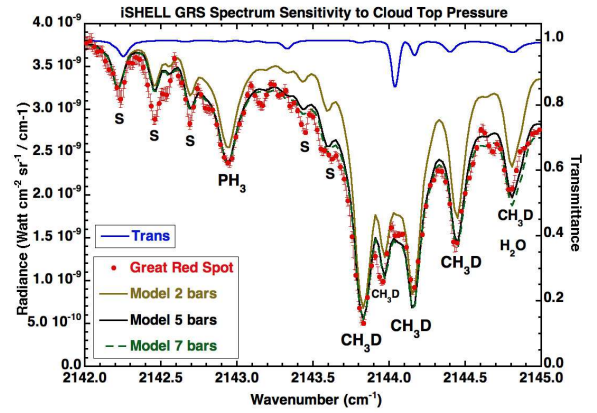


Figure 7. Comparison between IRTF / iSHELL spectrum of the Great Red Spot at $4.66\ \mu\text{m}$ and three models that differ only in the pressure of the lower boundary, assumed to be an opaque cloud. A model with an opaque cloud at 2 bars is excluded, while in this spectral region models with an opaque cloud at 5 and 7 bars fit equally well.

In Figure 9 we explore the sensitivity of the GRS spectrum to the fraction of reflected sunlight from the upper cloud layer. Changes in this parameter affect the strength of Fraunhofer lines as well as CH_3D absorption features. **The best fit to the $4.66\text{-}\mu\text{m}$ spectrum requires a mixture of 0.6 ± 0.1 reflected sunlight and 0.4 ± 0.1 thermal emission. This corresponds to an upper cloud albedo of 0.17 ± 0.03 .** Models with fractions of 0.4 and 0.8 reflected sunlight (corresponding to albedos of 0.115 and 0.23) do not fit the CH_3D absorption lines, nor the PH_3 feature at $2143\ \text{cm}^{-1}$ nearly as well.

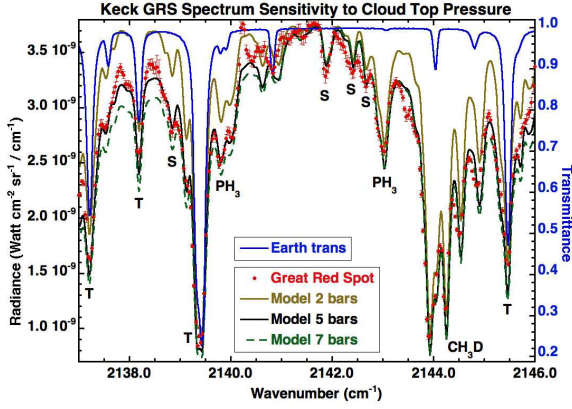


Figure 8. Comparison between Keck / NIRSPEC spectrum of the Great Red Spot at $4.66 \mu\text{m}$ and three models that differ only in the pressure of the lower boundary. A model with an opaque cloud at 2 bars is excluded. The model with an opaque cloud at 5 bars fits the region near 2138 cm^{-1} better than the model with an opaque cloud at 7 bars.

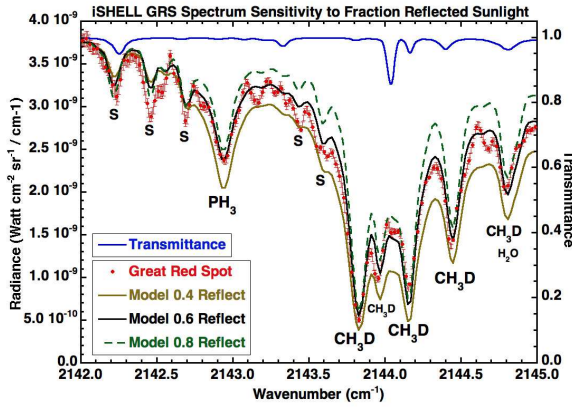


Figure 9. Comparison between IRTF / iSHELL spectrum of the Great Red Spot and three models that differ in the fraction of reflected sunlight at $4.66 \mu\text{m}$. This parameter affects the strength of solar lines (S) as well as CH_3D features. The model with 0.4 reflected sunlight requires an upper cloud albedo of 0.115. The model with 0.8 reflected sunlight requires an upper cloud albedo of 0.23. **The best fit has an albedo of 0.17 ± 0.03 , resulting in a fraction of 0.6 ± 0.1 reflected sunlight.**

3.1.2. Upper cloud level

The $5\text{-}\mu\text{m}$ spectrum of Jupiter's Great Red Spot is a combination of thermal emission and reflected sunlight. To isolate the reflected component we used the very strong $2\nu_2$ band of gaseous NH_3 at $5.32 \mu\text{m}$ (1880 cm^{-1}). Here, absorption by NH_3 is so strong that the thermal component is essentially

zero. The continuum level is set by the albedo of the reflecting level (0.17 ± 0.03), which we measured at $4.66 \mu\text{m}$ using Fraunhofer lines. These lines are blended with NH_3 and so we cannot use their strength to derive the albedo of the GRS at $5.32 \mu\text{m}$. We adopted an albedo of 0.17 ± 0.03 across the entire $5\text{-}\mu\text{m}$ spectrum, a reasonable assumption because the imaginary index of refraction for NH_3 ice is between 0.01 and 0.001 in this wavelength range (Martonchik et al. 1984).

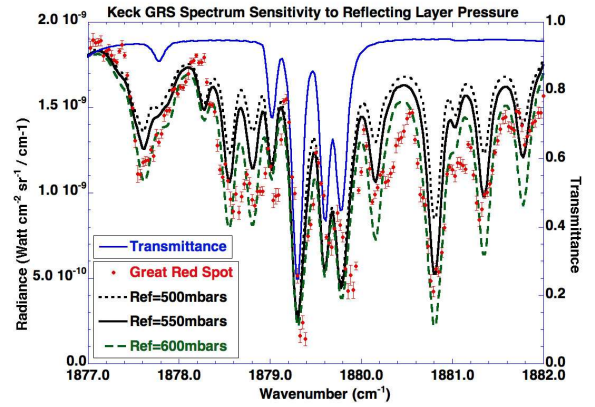


Figure 10. Comparison between NIRSPEC spectrum of the Great Red Spot at $5.32 \mu\text{m}$ and three models with reflecting layers at 500, 550, and 600 mbars. All features are due to ammonia except for the telluric water lines shown in blue. The mole fraction of NH_3 is 14, 30, and 60 ppm at these levels. **The best fit is for a reflecting layer at 570 ± 30 mbars.**

In Fig. 10 we show the spectrum of the Great Red Spot where the strongest NH_3 features occur. These absorption features are sensitive to the column of NH_3 above the reflecting layer. However, NH_3 is condensing so we cannot measure the vertical profile of ammonia and the pressure of the reflecting layer separately. Therefore, we assume that the mole fraction of NH_3 is 200 ppm in the deep atmosphere (see Section 3.3) and follows the saturated vapor pressure relation for pressures less than 700 mbars. We used a temperature profile obtained from the Galileo Probe (Seiff et al. 1998). Although this profile was not measured in the GRS, there is good agreement between the Probe temperature of 130.0 K at 468 mbars and a

value of 130 K at 400 mbars within the GRS derived from mid-IR mapping (Fletcher et al. 2016). We compare the GRS spectrum with three models with reflecting layers at 500, 550, and 600 mbars. **The best fit to all NH_3 features has a reflecting layer at 570 ± 30 mbars where the NH_3 mole fraction is 40 ppm. If NH_3 is sub-saturated, the reflecting layer would be somewhat deeper (e.g. for 70% relative humidity, the NH_3 mole fraction would be 40 ppm at 600 mbars).** This is consistent with a cloud composed of ammonia ice.

3.1.3. Middle cloud level

Evidence for a cloud layer in the Great Red Spot between the ammonia and water clouds requires a combination of $5\text{-}\mu\text{m}$ and $7\text{-}\mu\text{m}$ data. Since the Earth's atmosphere is opaque near $7\text{ }\mu\text{m}$, it is necessary to use spacecraft data. We used thermal infrared spectra from the CIRS investigation on the Cassini mission acquired as it flew by Jupiter en route to Saturn. As described in Section 2, we selected CIRS spectra from an NEB Hot Spot for comparison with the Great Red Spot. Of particular interest is a window to Jupiter's troposphere at $7.18\text{ }\mu\text{m}$ (1392 cm^{-1}) due to a minimum in CH_4 opacity. This window was first exploited by Matcheva et al. (2005) to map Jupiter's belt-zone structure with CIRS data. The contribution function for a cloud-free atmosphere at 1392 cm^{-1} peaks near 1.3 bars. Thus, this spectral window sounds the atmosphere between the expected levels for ammonia clouds and ammonium hydrosulfide clouds on Jupiter. This allowed Matcheva et al. (2005) to study the variable opacity of NH_3 clouds on Jupiter without any confusion from deeper clouds.

A comparison of the radiance of the Great Red Spot to an NEB Hot Spot at 1392 cm^{-1} will give a rough estimate of the transmittance of the ammonia clouds within the GRS. In Fig. 11 we compare the GRS spectrum to that of the NEB Hot Spots. The radiance scale for the GRS in this spectral region is 0.25 times that of the NEB Hot Spot. The central peak at 1392 cm^{-1} is a continuum region

bracketed by CH_4 absorption lines throughout the region between 1380 and 1435 cm^{-1} . If the NEB Hot Spots are cloud-free for pressures less than 1.3 bars, then the transmittance of NH_3 clouds above the GRS would be 0.25 to match the radiance at 1392 cm^{-1} .

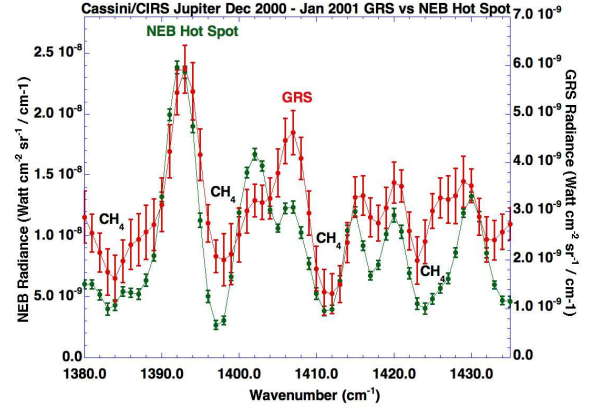


Figure 11. Comparison between Cassini / CIRS spectra of the Great Red Spot and a Hot Spot in the North Equatorial Belt. The radiance scale for the GRS is 0.25 times that of the Hot Spot. These spectra have numerous CH_4 absorption lines. The continuum at 1392 cm^{-1} sounds the 1.3-bar level, well below the NH_3 clouds.

To provide indirect evidence for the existence of ammonium hydrosulfide clouds in the Great Red Spot, we combine information that we have learned from studying GRS spectra at $5\text{ }\mu\text{m}$ and at $7.18\text{ }\mu\text{m}$. We can use laboratory measurements of the imaginary index of refraction (k) of ammonia ice at 80 K by Howett et al. (2007) to constrain the transmittance of the NH_3 cloud at $5\text{ }\mu\text{m}$. **The value of k is 3.32×10^{-3} at 1400 cm^{-1} , 1.13×10^{-2} at 1900 cm^{-1} , and has values of 1.5×10^{-3} or less from 1950 to 2200 cm^{-1} .** Thus, ammonia ice is less absorbing across the $5\text{-}\mu\text{m}$ window than at $7.18\text{ }\mu\text{m}$, except near the strong NH_3 gas (and ice) absorption band at $5.3\text{ }\mu\text{m}$. Our model of the GRS requires a total cloud transmittance of 0.0185 at $4.66\text{ }\mu\text{m}$ above the line formation region which lies between 2 and 5 bars. From $5\text{-}\mu\text{m}$ data alone, this cloud could be entirely at the ammonia cloud level. By combining CIRS data at $7.18\text{ }\mu\text{m}$ with ground-based data at

$5\ \mu\text{m}$, we suggest that the Great Red Spot contains clouds at both the expected levels for NH_3 and NH_4SH clouds. Adopting a value for the transmittance for the NH_3 cloud at $4.66\ \mu\text{m}$ equal to that at $7.18\ \mu\text{m}$ (0.25) would require an NH_4SH cloud transmittance of 0.074. Given that the NH_3 ice cloud will be less absorbing at $4.66\ \mu\text{m}$, the lower cloud must be the dominant absorber, with a transmittance less than or equal to 0.074. Thus, we conclude that the Great Red Spot **most likely** contains NH_4SH clouds that are more optically thick at $5\ \mu\text{m}$ than the overlying NH_3 clouds.

3.1.4. Summary of Cloud Model

We present a schematic of our three-layer cloud model of the Great Red Spot in Fig. 12. The transmission of each cloud layer is shown next to a Galileo temperature, pressure profile. Thermal emission from the GRS originates at 5 bars from an opaque water cloud. It then traverses a thick NH_4SH cloud, followed by a thinner NH_3 cloud. **A second component of the GRS spectrum comes from sunlight reflecting off the NH_3 cloud with an albedo of $17\pm3\%$. Fraunhofer lines provide evidence for this reflected component and their depth constrains the outgoing radiance to be $60\pm10\%$ reflected sunlight and $40\mp10\%$ thermal emission at $4.66\ \mu\text{m}$.**

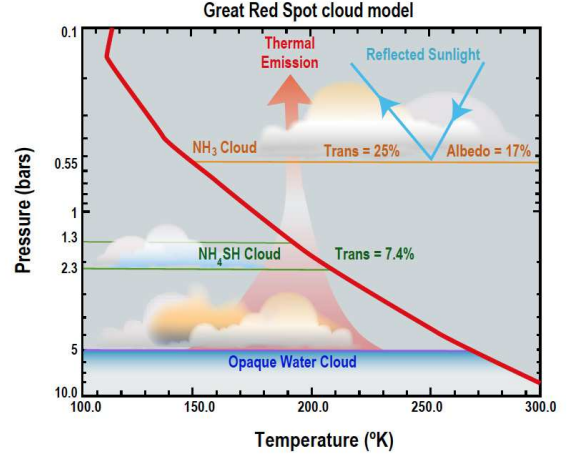


Figure 12. Simplified cloud model for the Great Red Spot. The three cloud layers are shown **with significant opacity at 0.57 ± 0.03 bar, ~ 1.3 to 2.3 bars, and 5 ± 1 bars** next to a Galileo Probe temperature, pressure profile. **The transmittances of these same three clouds are 25%, 7.4%, and 0%, respectively. The upper cloud has an albedo of $17\pm3\%$.**

3.2. Gas abundances

3.2.1. Water abundance

We next modeled the Great Red Spot between 4.95 and $4.99\ \mu\text{m}$ (2006 - $2020\ \text{cm}^{-1}$) to constrain the water abundance. We used iSHELL data in this region rather than NIRSPEC due to the higher Doppler shift and spectral resolution. We used the cloud model described in the previous section and varied one model parameter. We assumed a saturated H_2O profile above an opaque cloud at 2, 5, and 7 bars. Due to a Doppler shift of $28\ \text{km/sec}$ jovian H_2O lines in the GRS are shifted by $0.19\ \text{cm}^{-1}$ to the left of telluric water lines in Figures 13 and 14.

Note that the observed H_2O line profiles at 2007.5, 2009.1, 2016.4, and 2018.0 are broader than the telluric H_2O features. The model with an opaque base at 2 bars (gold curve) fails to fit the spectrum because nearly all of the jovian H_2O is frozen out at these levels with temperatures less than 209 K. Models with lower boundaries at 5 bars (274 K) and 7 bars (304 K) fit the $4.96\text{-}\mu\text{m}$ spectrum equally well. The spectrum of the GRS at $4.67\ \mu\text{m}$ ($2138\ \text{cm}^{-1}$) is also sensitive to H_2O . The spectrum shown in Fig. 8 is matched

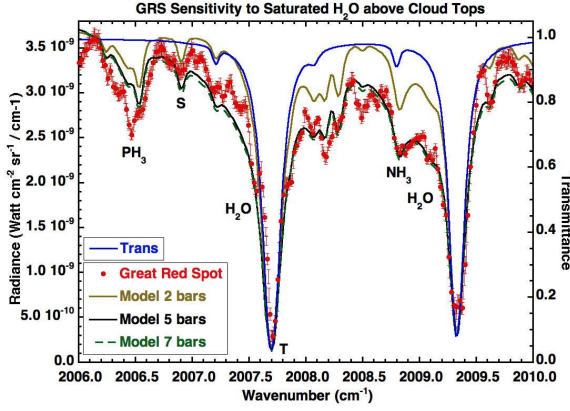


Figure 13. Comparison between iSHELL spectrum of the Great Red Spot at $4.98 \mu\text{m}$ and three models that differ only in the pressure of the lower boundary, assumed to be an opaque cloud. A saturated H_2O profile is used for all 3 models. The model with an opaque cloud at 2 bars is excluded, while models with an opaque cloud at 5 and 7 bars fit the spectrum equally well.

better by a model with an opaque cloud at 5 bars, rather than 7 bars. Thus, we adopt a model with a saturated H_2O distribution above an opaque water cloud at 5 bars.

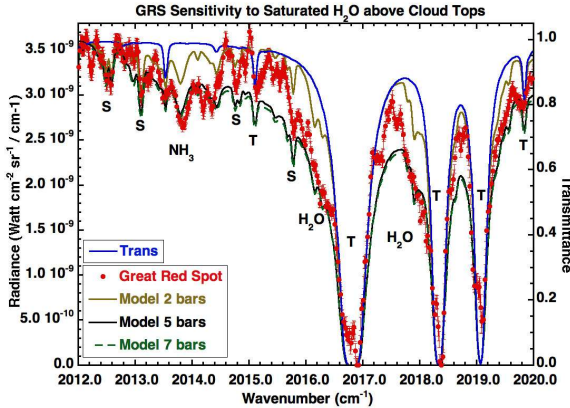


Figure 14. Same as in Fig. 13, but for H_2O lines at $4.96 \mu\text{m}$. Models with an opaque cloud at 5 and 7 bars fit the wings of H_2O lines at 2016.4 and 2018.0 cm^{-1} equally well, whereas the 2-bar model does not fit the spectrum.

3.2.2. Ammonia abundance

We used the iSHELL spectrum of the Great Red Spot at $5.16 \mu\text{m}$ to constrain the deep abundance of ammonia. We present in Fig. 15 a portion of the GRS spectrum between 1937 and 1941 cm^{-1} .

The two strong absorption lines of NH_3 with rest frequencies of 1938.97 and 1939.56 belong to the $2\nu_2$ band. They sound the 3-bar level on Jupiter. These lines are Doppler-shifted by 0.18 cm^{-1} in the spectrum of the GRS. Using the cloud model described earlier, we calculated the spectrum for three abundances of NH_3 , namely, 100, 200, and 400 ppm. The model with 200 ppm provides the best fit to the spectrum. This same abundance fits two weaker NH_3 features at 2008.8 cm^{-1} (Fig. 13) and 2013.8 cm^{-1} (Fig. 14). **We adopt a value of 200 ± 50 ppm NH_3 in the Great Red Spot.**

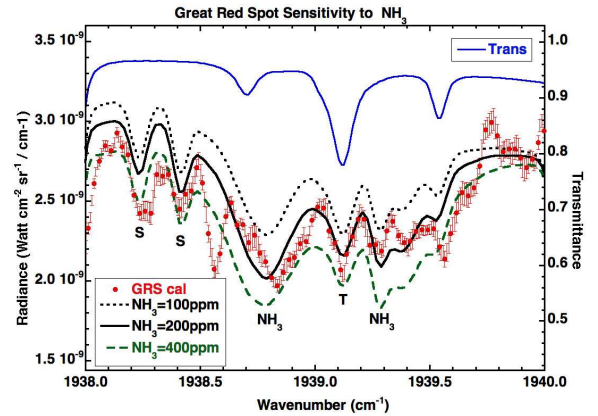


Figure 15. Comparison between iSHELL spectrum of the Great Red Spot at $5.16 \mu\text{m}$ and three models with NH_3 mole fractions of 100, 200, and 400 ppm in the deep atmosphere. **We adopt a value of 200 ± 50 ppm NH_3 in the GRS.**

In Fig. 16 we present the vertical profiles of H_2O and NH_3 that provide the best fit to our $5\text{-}\mu\text{m}$ spectra. Water vapor follows a saturated profile above the water cloud at 5 bars. Ammonia has a mole fraction of 200 ppm in the deep atmosphere and is assumed to follow a saturated profile for pressures less than 0.7 bars.

3.2.3. Phosphine abundance

We used the iSHELL spectrum of the Great Red Spot at $4.66 \mu\text{m}$ to constrain the deep abundance of phosphine (PH_3). We present in Fig. 17 a portion of the GRS spectrum between 2142 and 2145 cm^{-1} . Using the cloud model described earlier, we calculated the spectrum for three abundances of PH_3 , namely, 0.4, 0.8, and 1.2 ppm for

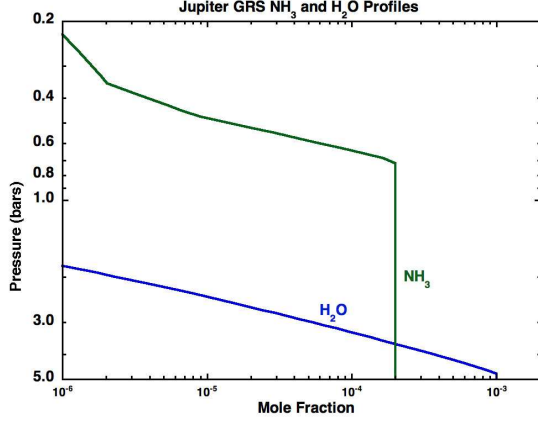


Figure 16. Vertical profiles of H_2O and NH_3 in the Great Red Spot used to calculate synthetic spectra. The water mole fraction is 1000 ppm at 5 bars and it follows a saturated profile above this level. Ammonia is 200 ppm in the deep atmosphere. It begins to condense at 0.7 bars and it follows a saturated profile in the upper troposphere.

pressures greater than 0.7 bar. Our PH_3 profile falls off in the upper troposphere and is zero in the stratosphere in order to be consistent with previous studies (e.g. Irwin et al. (2004), and Fletcher et al. (2010)); however, the $4.66\text{-}\mu\text{m}$ spectrum is not sensitive to pressures less than 0.7 bar. The model with 0.8 ppm provides the best fit to the spectrum. **We adopt a value of 0.8 ± 0.2 ppm PH_3 in the Great Red Spot.**

In Fig. 18 we modeled a portion of the warm collar surrounding the Great Red Spot located $3.3''$ west of its center. In order to fit the broad CH_3D absorption lines, there must be no significant cloud opacity at the predicted level of the water cloud. We used the H_2O profile measured by the Galileo Probe for pressures greater than 4.5 bars. There are four PH_3 absorption lines in this portion of the spectrum. The best fit to the Warm Collar spectrum requires 0.4 ppm PH_3 , which is half the abundance required to fit the GRS. **We adopt a value of 0.4 ± 0.1 ppm PH_3 in the Warm Collar.**

3.2.4. Germane abundance

We used the iSHELL spectrum of the Great Red Spot at $4.66\text{ }\mu\text{m}$ to constrain the abundance

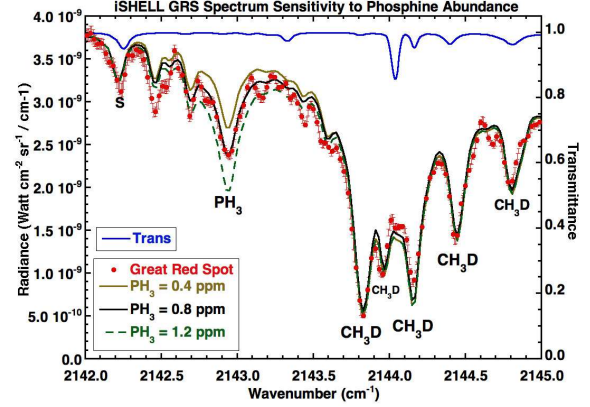


Figure 17. Comparison between iSHELL spectrum of the Great Red Spot and three models with PH_3 mole fractions of 0.4, 0.8, and 1.2 ppm in the deep atmosphere. **We adopt a value of 0.8 ± 0.2 ppm PH_3 in the GRS.**

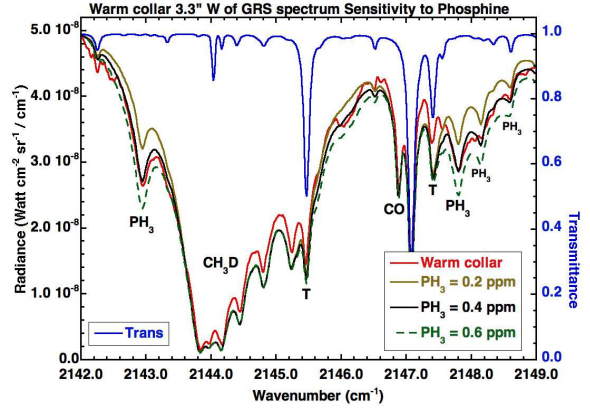


Figure 18. Comparison between iSHELL spectrum of the Warm Collar and three models with PH_3 mole fractions of 0.2, 0.4, and 0.6 ppm in the deep atmosphere. **We adopt a value of 0.4 ± 0.1 ppm PH_3 in the Warm Collar.**

of germane (GeH_4). We present in Fig. 19 and Fig. 20 portions of the GRS spectrum near 2139 and 2150 cm^{-1} . We detect all 5 naturally occurring isotopes of germanium in GeH_4 . Assuming terrestrial isotopic ratios, we calculated the spectrum for three abundances of GeH_4 : 0.3, 0.4, and 0.6 ppb. The model with 0.3 ppb fits an absorption feature of $^{74}\text{GeH}_4$ at 2139 cm^{-1} , while 0.4 ppb is required to fit features near 2150 cm^{-1} . **We therefore adopt a value of 0.35 ± 0.05 ppb for GeH_4 in the Great Red Spot.**

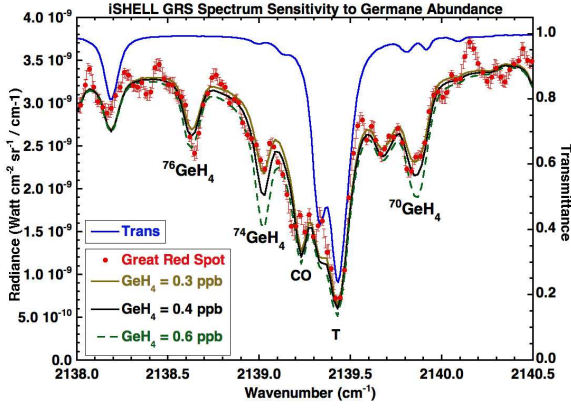


Figure 19. Comparison between iSHELL spectrum of the Great Red Spot and three models with GeH_4 mole fractions of 0.3, 0.4, and 0.6 ppb. Three isotopologues of GeH_4 are shown. The model with 0.3 ppb GeH_4 provides the best fit to this portion of the spectrum.

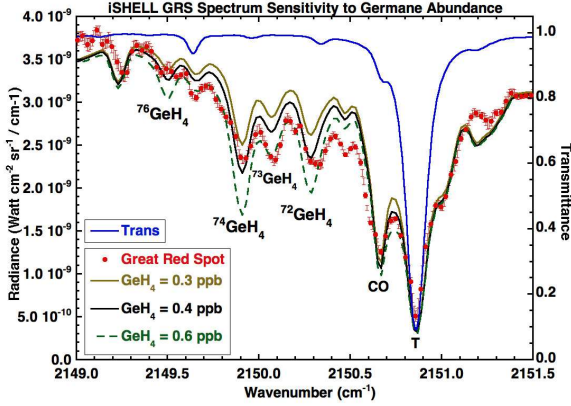


Figure 20. Comparison between iSHELL spectrum of the Great Red Spot and three models with GeH_4 mole fractions of 0.3, 0.4, and 0.6 ppb. Four isotopologues of GeH_4 are shown. The model with 0.4 ppb GeH_4 provides the best fit to this portion of the spectrum.

3.2.5. Carbon monoxide abundance

We used the iSHELL spectrum of the Great Red Spot at $4.66 \mu\text{m}$ to constrain the tropospheric abundance of carbon monoxide. We present in Fig. 21 and Fig. 22 two portions of the GRS spectrum near 2147 and 2151 cm^{-1} . Here the combination of high Doppler shift (28 km/sec) and high spectral resolution (0.06 cm^{-1}) permits a clean separation of 0.20 cm^{-1} (more than 3 resolution elements) between the telluric CO line, marked T, and the jovian feature. Using the cloud model described earlier, we calculated the spectrum for

three tropospheric abundances of CO: 0.4, 0.8, and 1.2 ppb . The model with 0.8 ppb in the deep atmosphere provides the best fit to the spectrum. We adopt a value of $0.8 \pm 0.2 \text{ ppb CO}$ in the troposphere. All models used the stratospheric profile for CO of Bézard et al. (2002).

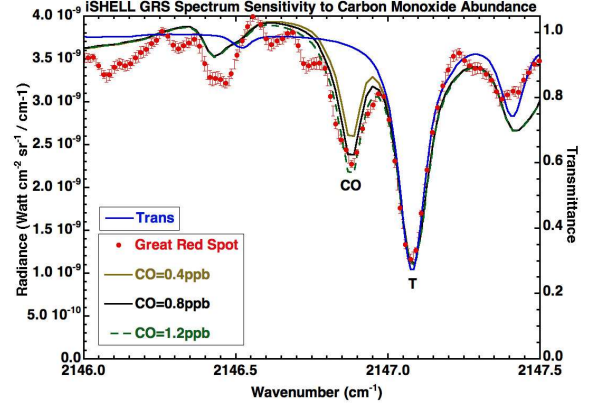


Figure 21. Comparison between iSHELL spectrum of the Great Red Spot and three models with CO mole fractions of 0.4, 0.8, and 1.2 ppb in the troposphere. The R0 line of CO on Jupiter is well separated from its telluric counterpart (T). We adopt a value of $0.8 \pm 0.2 \text{ ppb CO}$ in the troposphere.

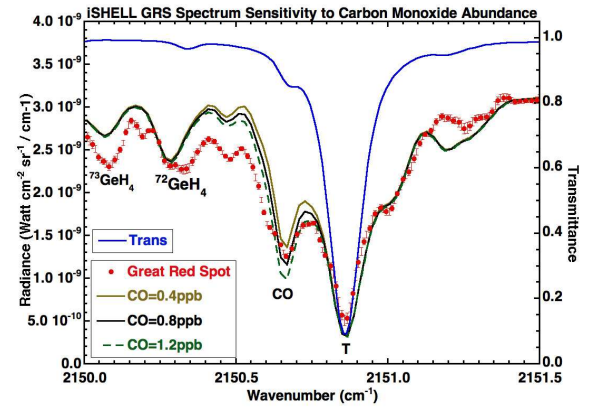


Figure 22. Same as Fig. 21 for the R1 line of CO. We adopt a value of $0.8 \pm 0.2 \text{ ppb CO}$ in the troposphere.

4. DISCUSSION

4.1. Cloud Structure

Using a simplified 3-cloud model, we obtained a good fit to the $5\text{-}\mu\text{m}$ spectrum of the Great Red Spot using a framework that is consistent with thermochemical models. Future studies can build

on and test this framework by adding cloud microphysics, which would include modeling the vertical extent of each cloud layer. In addition, improved models would include wavelength-dependent absorption coefficients of NH_3 ice and NH_4SH ice across the $5\text{-}\mu\text{m}$ window, and incorporate scattering.

Our discovery of an opaque cloud at 5 ± 1 bars (almost certainly a water cloud) in the Great Red Spot may suggest that the vortex extends much deeper than the water cloud layer. [Marcus et al. \(2013\)](#) developed a model of secondary circulation within jovian anticyclones that maintains their key thermodynamic features: a high-pressure core with its associated geostrophic winds, sandwiched between a cold, high-density lid at the top of the vortex, and a warm, low-density anomaly at the base of the vortex. The cold lid in this scenario is a well-known observational feature ([Cheng et al. 2008](#); [Fletcher et al. 2010](#)), and [Wong et al. \(2011\)](#) found that static stability measurements and models agreed with vortex models at the upper tropospheric levels where the cold lid is seen. [Wong et al. \(2011\)](#) also found that the low-density anomaly at the base of the vortex is consistent with stratification produced by condensation of a supersolar water cloud. If the GRS indeed had its base in the water cloud layer, then the warm, low-density anomaly there should generally inhibit water cloud formation, a scenario that is contradicted by our results in Figures 7 and 8. In fact, if the [Marcus et al. \(2013\)](#) model holds, our observation of 5-bar water clouds in the GRS may suggest that the vortex midplane lies below the 5-bar level, so that the water cloud layer is within the upper half of the vortex, where the secondary circulation is dominated by upwelling. Such a large vertical extent would also be consistent with preliminary Juno Microwave Radiometer observations of the GRS ([Li et al. 2017a](#)), as well as dynamical simulations showing that the vortex can extend well into the free convective zone ([Chan & Mayr 2013](#)).

Our derived pressure of the reflecting layer at 570 ± 30 mbars in the GRS is consistent with previous studies of upper clouds by [Banfield et al. \(1998\)](#), but it is inconsistent with a layer at 900 mbars as suggested by [Simon-Miller et al. \(2001\)](#). Our evidence for a thick middle cloud is consistent with near-infrared spectra from Galileo NIMS. [Irwin et al. \(2001\)](#) investigated the question of whether the NH_3 cloud or a deeper cloud is responsible for the observed variability in the brightness of Jupiter at $5\text{ }\mu\text{m}$. They studied Galileo NIMS data and found an anti-correlation between the brightness of Jupiter at $5\text{ }\mu\text{m}$ and that at $1.58\text{ }\mu\text{m}$. Irwin et al. used a reflecting layer model to fit NIMS spectra from 0.7 to $2.5\text{ }\mu\text{m}$ of belts (bright at $5\text{ }\mu\text{m}$, dark at $1.58\text{ }\mu\text{m}$) and zones (dark at $5\text{ }\mu\text{m}$, bright at $1.58\text{ }\mu\text{m}$). Successful models required variations in cloud opacity to lie deeper than 1 bar. Their model of the Great Red Spot from NIMS data required increased NH_3 cloud opacity to fit 0.7 to $1.0\text{ }\mu\text{m}$ as well as increased cloud opacity between 1 and 2 bars to fit the spectrum from 1.0 to $2.5\text{ }\mu\text{m}$. Thus, Irwin et al. provided evidence for two cloud layers in the GRS, but they could not determine the optical depths of each cloud separately.

The cloud structure derived for the GRS in this study is fairly similar to that derived for a cloudy feature in the South Tropical Zone (STZ) by [Bjoraker et al. \(2015\)](#). In that paper we argued that mass flux into the upper cloud layers of the STZ is not dominated by horizontal transport, as suggested by [Showman & de Pater \(2005\)](#), but instead is driven by vertical transport from below. Jupiter's circulation in zones (and now in the Great Red Spot) therefore maintains the same sign of upwelling/downwelling across the full 0.5-5 bar weather layer. The same sign of upwelling/downwelling over this large an extent was also derived by [de Pater et al. \(2010\)](#) from 5-micron bright rings around vortices. These authors suggested that vortices must extend vertically from at least the 4 to 7-bar level up to the tropopause.

This seems to be the case for the Great Red Spot as well.

4.2. Water abundance and the O/H ratio

This study constitutes the first detection of gaseous water in Jupiter’s Great Red Spot. Water follows a saturated profile in the GRS, similar to that of a cloudy feature in the STZ, but unlike the highly depleted H_2O profile observed in Hot Spots (Bjoraker et al. 2015). The pressure that we derived for the opaque lower cloud is useful for understanding the vertical extent and dynamics of the GRS. In addition, it provides a constraint on the deep water abundance of Jupiter as a whole, and therefore its O/H ratio, assuming that the lower cloud is, in fact, composed of water. The base of the water cloud is sensitive to the deep abundance of water because higher abundances lead to condensation at deeper levels. Our data provide the level of the cloud top, not the cloud base. Since the top is at a higher altitude than the base, cloud top constraints provide lower limits to the pressure of the cloud base, or, lower limits to the deep abundance of water. The GRS spectrum requires a water cloud top at $P \geq 5$ bar. The cloud base is therefore found at $P > 5$ bars. Following Fig. 1 in Wong et al. (2008), a cloud base at 5 bar corresponds to an O/H ratio of $1.1 \times$ solar (corrected to the new solar O/H ratio of Asplund et al. 2009). The O/H lower limit of $1.1 \times$ solar is consistent with, and more constraining than, the Galileo Probe lower limit of $0.48 \pm 0.16 \times$ solar (Wong et al. 2004). Our observations support either solar or super-solar enrichments of water in Jupiter, providing somewhat better constraints to planetary formation models (Gautier et al. (2001), Hersant et al. (2004), and Wong et al. (2008)).

4.3. Ammonia abundance

Our retrieved NH_3 abundance of 200 ± 50 ppm in the Great Red Spot for pressures greater than 0.7 bars may be compared with other $5\text{-}\mu\text{m}$ studies. Giles et al. (2017b) obtained $5\text{-}\mu\text{m}$ spectra of Jupiter using the CRIRES instrument on the

Very Large Telescope at the European Southern Observatory in Chile. They did not observe the Great Red Spot, but they did report the latitudinal variation of NH_3 acquired using spectra aligned north-south on Jupiter’s central meridian. They found NH_3 mixing ratios less than 200 ppm at 1.6 bars for all latitudes using a strong NH_3 absorption feature (at 1939 cm^{-1} ; see Fig. 15), and larger values for NH_3 at 3.3 bars using a weaker feature (at 1929 cm^{-1}). Some differences between this group’s work and our results may be due to the very different treatments of cloud opacity in the two studies. Giles et al. (2017b) initially used a single compact cloud layer at 0.8 bars. Later, they examined the effect of an additional cloud at 5 bars, following Bjoraker et al. (2015). They also did not include sunlight reflected from an upper cloud layer. Giles et al. (2017b) obtained 150 ppm NH_3 at 1.6 bars increasing to 250 ppm at 3.3 bars for a region of Jupiter at 20° South latitude on Jupiter, which is the latitude of the GRS. This is in good agreement with our results. However, this agreement may be fortuitous if NH_3 varies with longitude due to local dynamics.

Using microwave observations of Jupiter from the Very Large Array radio telescope, de Pater et al. (2016) obtained longitude-resolved maps with sufficient spatial resolution (1200 km) to resolve the Great Red Spot. Using microwave channels from 5.49 to 17.38 GHz (1.7 to 5.5 cm), they obtained a vertical profile for NH_3 at the center of the GRS of 200 ppm at pressures less than 1.5 bars increasing to 570 ppm at deeper levels. Contribution functions for these wavelengths cover roughly 0.6 to 6 bars in Jupiter’s troposphere, depending on the exact NH_3 profile (see Fig. 1). In a future paper we plan to model the GRS using an updated (and recalibrated) microwave spectrum between 5 and 25 GHz. We plan to include microwave opacity by clouds in addition to absorption by NH_3 , H_2S , and H_2O (e.g., de Pater & Mitchell (1993); de Pater et al. (2005)) for comparison with the current study at $5\text{ }\mu\text{m}$.

Our deep (0.7 - 5 bars) NH_3 concentration of 200 ppm is a low value, and has implications for the vertical profile of NH_3 in Jupiter's atmosphere both inside and outside of the GRS. Assuming that the internal circulation of the GRS is somewhat isolated from its exterior, the 200 ppm concentration of NH_3 is likely to persist all throughout the interior of the vortex, even below the water cloud that limits our observational sensitivity to pressures less than 5 bars. Our deep GRS value is lower than the concentration of about 400 ppm in the Galileo Probe entry site near 5 bars (Hanley et al. 2009), lower than the concentration of 570 ppm at the deepest levels of the Galileo Probe entry site (Wong et al. 2004), and lower than the deepest concentration of 360 ppm derived from Juno MWR data (Li et al. 2017b).

Measurements of the NH_3 profile in the Galileo Probe Entry Site, a $5\text{-}\mu\text{m}$ Hot Spot, found a gradually increasing concentration of NH_3 , down to a well-mixed level near 8 bars, coincident with a layer of higher static stability (Magalhães et al. 2002). The 8-bar level possibly represented the ammonia cloud base (Wong 2009) after having been deflected downward by the Rossby wave system responsible for creating these Hot Spots (Showman & Ingersoll 1998; Friedson 2005). This scenario implied that Jupiter's NH_3 concentration should be around 570 ppm everywhere below the cloud base, a high value that was difficult to reconcile with disk-averaged microwave spectra (de Pater et al. 2001). But spatially resolved microwave spectroscopy can explain these discrepancies by showing that high (570 ppm) ammonia below the cloud base indeed occurs in plumes located near (and to the south of) $5\text{-}\mu\text{m}$ Hot Spots, while other regions of the planet are less ammonia-rich (de Pater et al. 2016). This is qualitatively consistent with the Juno MWR findings of depleted (200 ppm) ammonia in the 3 - 10 bar range, over a wide range of latitudes [10 - 40° S and 20 - 40° N, (see Li et al. (2017b))]. Although NH_3 within the GRS should be vertically mixed by the inter-

nal circulation of the vortex, the composition of the air within the GRS should generally reflect the composition of its surroundings.

4.4. Phosphine abundance

Phosphine is a disequilibrium species in Jupiter's atmosphere. Equilibrium models by Fegley & Lodders (1994) show that PH_3 should be abundant at 1500 K in the deep atmosphere, but it would be converted to P_4O_6 at colder levels. The presence of PH_3 at the 5-bar level requires vertical transport from great depth on a time scale faster than the chemical conversion to P_4O_6 with an eddy diffusion coefficient (K) on the order of $10^8 \text{ cm}^2 \text{ sec}^{-1}$. The value of K was constrained by measurements of PH_3 primarily in Hot Spots (e.g. Bjoraker et al. (1986a)). Our new measurements of PH_3 in the GRS indicate that vertical transport rates in the GRS may be higher than those in Hot Spots. **An alternate disequilibrium model was developed by Wang et al. (2016). In this model PH_3 is converted to H_3PO_4 instead of P_4O_6 . They found that PH_3 is relatively insensitive to K , and thus should not vary with location on Jupiter.**

Our PH_3 abundance in the GRS at the 5-bar level (0.8 ± 0.2 ppm) is a factor of 2 higher than in the warm collar surrounding the GRS (0.4 ± 0.1 ppm). Bjoraker et al. (2015) measured 0.45 ppm PH_3 in an SEB Hot Spot at 17°S and 0.7 ppm PH_3 in a region in the STZ at 32°S. These four measurements provide evidence for an enhancement in PH_3 at the 5-bar level in cloudy regions (GRS and STZ) compared with regions lacking an opaque water cloud (an SEB Hot Spot and the Warm Collar). This may be a consequence of enhanced convection in cloudy regions on Jupiter. These measurements are not consistent with the predictions of the model developed by Wang et al. (2016).

Fletcher et al. (2016) reported 1.2 ppm PH_3 over the Great Red Spot at 0.5 bars using IRTF/TEXES data at $10 \mu\text{m}$. The PH_3 abundance fell off to 0.4 to 0.6 ppm in the warm collar surrounding the GRS. This falloff from the center of the GRS to the

warm collar is in qualitative agreement with our measurements. However, our 0.8-ppm value for PH_3 at 5 bars is lower than the value at 0.5 bars (1.2 ppm) obtained using absorption features at $10\ \mu\text{m}$. Fletcher et al. (2009) first noticed the discrepancy between PH_3 retrievals at 5 and $10\ \mu\text{m}$. A larger abundance of PH_3 at 0.5 bars than at 5 bars would be inconsistent with the disequilibrium model. These authors attributed this discrepancy to possible errors in the line strengths of PH_3 . **This discrepancy motivated a laboratory study of PH_3 line strengths at $5\ \mu\text{m}$ (Malathy Devi et al. 2014). The newer measurements of PH_3 line intensities are about 7% higher than the older lab data of Tarrago et al. (1992) that are on the GEISA line atlas (Jacquinet-Husson et al. 2005) that we used in this study. This is not sufficient to explain the 50% difference between PH_3 mole fractions derived from 5 and $10\ \mu\text{m}$ data.** Thus, this problem has yet to be resolved.

4.5. Germane abundance

Germane is also a disequilibrium species in Jupiter's atmosphere. Models by Fegley & Lodders (1994) and by Wang et al. (2016) show that GeH_4 should be abundant at 2000 K in the deep atmosphere, but it would be converted to GeS at colder levels. The presence of GeH_4 at the 5-bar level requires vertical transport from great depth with an eddy diffusion coefficient similar to that obtained for PH_3 , $\approx 10^8\ \text{cm}^2\ \text{sec}^{-1}$. **Our retrieved value of $0.35 \pm 0.05\ \text{ppb}$ in the GRS** is compatible with this vertical transport model.

Giles et al. (2017a) observed Jupiter's South Equatorial Belt (SEB) at $5\ \mu\text{m}$ using the CRIRES instrument, as described above. They detected the strong Q-branch of the ν_3 band of GeH_4 as well as the R3, R6, and R7 features. The R6 feature at $4.65\ \mu\text{m}$ ($2150.5\ \text{cm}^{-1}$) is the same feature that we observed in the Great Red Spot (see Fig. 20). Since the SEB does not have an opaque water cloud (see Bjoraker et al. (2015)) the pressure in the line formation region at $4.65\ \mu\text{m}$ is higher than in the GRS. Therefore, absorption features due to vari-

ous isotopologues of GeH_4 are blended together in the SEB due to opacity broadening and pressure broadening by H_2 . By measuring GeH_4 in a cloudy region such as the GRS, we can spectrally separate each individual isotopologue. In Fig. 19 and Fig. 20 we show absorption features of all 5 isotopic variants in the GRS. These are $^{70}\text{GeH}_4$, $^{72}\text{GeH}_4$, $^{73}\text{GeH}_4$, $^{74}\text{GeH}_4$, and $^{76}\text{GeH}_4$. The terrestrial relative abundances of germanium isotopes are 20.6%, 27.5%, 7.8%, 36.5%, and 7.7% respectively (Berglund & Wieser 2011). We obtained line lists for all isotopologues of GeH_4 from R. Giles (private communication, see Giles et al. (2017a) for details).

Using the same CRIRES dataset, Giles et al. (2017a) measured the latitudinal variation of the strong Q-branch of GeH_4 on Jupiter. As with NH_3 , they found that it was difficult to separate the effects of spatially varying GeH_4 from variations in the deep cloud structure. They found that they could fix GeH_4 to 0.58 ppb, the value in the SEB, and allow the deep cloud to vary. Alternatively, they could allow GeH_4 to vary with latitude, or they could permit both to vary. Their best fit model required both gas abundances and the deep cloud to vary with GeH_4 mole fractions ranging from 0.25 to 0.7 ppb. They obtained 0.45 ppb at 20° South, in good agreement with our results for the GRS.

4.6. Carbon monoxide abundance

There are two sources for CO on Jupiter. An external source of oxygen from meteoroids supplemented by large impacts such as from comet Shoemaker-Levy 9 results in the production of CO in Jupiter's stratosphere (Bézar et al. 2002). The second source of CO comes from CH_4 and H_2O in the deep atmosphere. Methane is the principal reservoir for carbon in Jupiter's reducing atmosphere, but at temperatures greater than 1000 K there is expected to be at least 1 ppb CO in chemical equilibrium with other carbon species including CH_4 . Methane is the only equilibrium carbon species at the colder temperatures (273 K) probed at $5\ \mu\text{m}$. The unexpected detection of CO on

Jupiter at 5 μm by Beer (1975) led to the development of a disequilibrium model in which CO is transported from depth faster than the time scale to convert it back to CH_4 (Prinn & Barshay 1977).

The Prinn and Barshay model was updated by Bézard et al. (2002) using improved reaction rates. The abundance of CO at 5 bars is proportional to the deep O/H ratio and depends on the eddy diffusion coefficient (K). Thus, the tropospheric abundance of CO can provide constraints on the deep water abundance as well as vertical transport rates. Bézard et al. (2002) measured 1.0 ± 0.2 ppb CO at 6 bars in an NEB Hot Spot.

Our abundance of 0.8 ± 0.2 ppb CO in the GRS is the first measurement of CO in a region of Jupiter with thick clouds. Our CO results, when combined with our measurements of PH_3 and GeH_4 , suggest that vertical transport rates in the GRS are similar to or somewhat higher than those in Hot Spots. A value of $10^8 \text{ cm}^2 \text{ sec}^{-1}$ for the eddy diffusion coefficient and 0.8 ppb CO would correspond to an O/H ratio of 4 times solar in the Bézard et al. (2002) model using the more recent solar abundances of Asplund et al. (2009). Bézard et al. (2002) estimated that K lies in a range between 4×10^7 and $4 \times 10^9 \text{ cm}^2 \text{ sec}^{-1}$. With these large uncertainties in K, Bézard et al. (2002) were only able to constrain Jupiter’s O/H ratio to be between 0.35 and 15 times solar (after correction to the solar value of Asplund et al. (2009)). Using our lower limit to O/H of 1.1 times solar derived from the pressure of the water cloud, we can narrow the range of the O/H ratio to be between 1.1 and 12 times solar.

Wang et al. (2015) proposed a new formulation for Jupiter’s eddy diffusion coefficient. They investigated the range of water enrichment required to fit Jupiter’s CO abundance using two different CO kinetic models. Using kinetics from Visscher & Moses (2011), and a CO abundance of 1 ppb from Bézard et al. (2002), they inferred O/H enrichments ranging between 0.1 and 0.75 times solar. Using an

alternate chemical kinetics model originally applied to hot Jupiters (Venot et al. 2012), they constrained the O/H ratio to be between 3 and 11 times solar. Our lower limit to O/H of 1.1 times solar derived from the pressure of the water cloud is consistent with the Venot et al. (2012) kinetic model, but not with the model of Visscher & Moses (2011). Using our CO value of 0.8 ppb in the Great Red Spot and the Venot et al. (2012) kinetic model, we obtain O/H enrichments between 2.4 and 9 times solar.

The data presented here were obtained using NASA’s Infrared Telescope Facility as well as using the Keck telescope. The W. M. Keck Observatory is operated as a scientific partnership among the California Institute of Technology, the University of California, and the National Aeronautics and Space Administration. The Observatory was made possible by the generous financial support of the W. M. Keck Foundation. The authors extend special thanks to those of Hawaiian ancestry on whose sacred mountain we are privileged to be guests. Without their generous hospitality, none of the observations presented would have been possible. This research was supported by the NASA Planetary Astronomy grant NNX14AJ43G to UC-Berkeley and NASA Solar System Observations grant NNX15AJ41G to NASA/Goddard and UC-Berkeley. Context maps used observations made with the NASA/ESA Hubble Space Telescope, obtained from the Data Archive at the Space Telescope Science Institute, which is operated by the Association of Universities for Research in Astronomy, Inc., under NASA contract NAS 5-26555. These observations are associated with programs GO-13067 and GO-14756.

Facilities: IRTF (iSHELL, SpeX, NSFCam, CSHELL), Keck:II (NIRSPEC), Cassini (CIRS, ISS), Voyager (IRIS), HST (WFC3), Galilep Probe (ASI)

REFERENCES

- Achterberg, R. K., Conrath, B. J., & Gierasch, P. J. 2006, *Icarus*, 182, 169, doi: [10.1016/j.icarus.2005.12.020](https://doi.org/10.1016/j.icarus.2005.12.020)
- Asay-Davis, X. S., Marcus, P. S., Wong, M. H., & de Pater, I. 2009, *Icarus*, 203, 164, doi: [10.1016/j.icarus.2009.05.001](https://doi.org/10.1016/j.icarus.2009.05.001)
- Asplund, M., Grevesse, N., Sauval, A. J., & Scott, P. 2009, *ARA&A*, 47, 481, doi: [10.1146/annurev.astro.46.060407.145222](https://doi.org/10.1146/annurev.astro.46.060407.145222)
- Atreya, S. K., & Romani, P. 1985, in *Planetary Meteorology*, ed. Hunt, G. E., 17–68
- Atreya, S. K., & Wong, A.-S. 2005, *SSRv*, 116, 121, doi: [10.1007/s11214-005-1951-5](https://doi.org/10.1007/s11214-005-1951-5)
- Bachet, G., Cohen, E. R., Dore, P., & Birnbaum, G. 1983, *Canadian Journal of Physics*, 61, 591, doi: [10.1139/p83-074](https://doi.org/10.1139/p83-074)
- Baines, K. H., Carlson, R. W., & Kamp, L. W. 2002, *Icarus*, 159, 74, doi: [10.1006/icar.2002.6901](https://doi.org/10.1006/icar.2002.6901)
- Baines, K. H., Carlson, R. W., Orton, G. S., & Galileo/NIMS Team. 1996, in *Bulletin of the American Astronomical Society*, Vol. 28, AAS/Division for Planetary Sciences Meeting Abstracts #28, 1136
- Banfield, D., Gierasch, P. J., Bell, M., et al. 1998, *Icarus*, 135, 230, doi: [10.1006/icar.1998.5985](https://doi.org/10.1006/icar.1998.5985)
- Beer, R. 1975, *ApJL*, 200, L167, doi: [10.1086/181923](https://doi.org/10.1086/181923)
- Berglund, M., & Wieser, M. E. 2011, *Pure Appl. Chem.*, 83, 397
- Bézard, B., Lellouch, E., Strobel, D., Maillard, J.-P., & Drossart, P. 2002, *Icarus*, 159, 95, doi: [10.1006/icar.2002.6917](https://doi.org/10.1006/icar.2002.6917)
- Birnbaum, G., & Cohen, E. R. 1976, *Canadian Journal of Physics*, 54, 593, doi: [10.1139/p76-064](https://doi.org/10.1139/p76-064)
- Bjoraker, G. L., Larson, H. P., & Kunde, V. G. 1986a, *ApJ*, 311, 1058, doi: [10.1086/164842](https://doi.org/10.1086/164842)
- . 1986b, *Icarus*, 66, 579, doi: [10.1016/0019-1035\(86\)90093-X](https://doi.org/10.1016/0019-1035(86)90093-X)
- Bjoraker, G. L., Wong, M. H., de Pater, I., & Ádámkovics, M. 2015, *ApJ*, 810, 122, doi: [10.1088/0004-637X/810/2/122](https://doi.org/10.1088/0004-637X/810/2/122)
- Boussin, C., Lutz, B. L., Hamdounia, A., & de Bergh, C. 1999, *JQSRT*, 63, 49, doi: [10.1016/S0022-4073\(98\)00134-4](https://doi.org/10.1016/S0022-4073(98)00134-4)
- Carlson, B. E., Rossow, W. B., & Orton, G. S. 1988, *Journal of Atmospheric Sciences*, 45, 2066, doi: [10.1175/1520-0469\(1988\)045<2066:CMOTGP>2.0.CO;2](https://doi.org/10.1175/1520-0469(1988)045<2066:CMOTGP>2.0.CO;2)doi: [10.1016/j.icarus.2005.03.004](https://doi.org/10.1016/j.icarus.2005.03.004)
- Carlson, R. W., Baines, K. H., Anderson, M. S., Filacchione, G., & Simon, A. A. 2016, *Icarus*, 274, 106, doi: [10.1016/j.icarus.2016.03.008](https://doi.org/10.1016/j.icarus.2016.03.008)
- Chan, K. L., & Mayr, H. G. 2013, *Earth and Planetary Science Letters*, 371, 212, doi: [10.1016/j.epsl.2013.03.046](https://doi.org/10.1016/j.epsl.2013.03.046)
- Cheng, A. F., Simon-Miller, A. A., Weaver, H. A., et al. 2008, *AJ*, 135, 2446, doi: [10.1088/0004-6256/135/6/2446](https://doi.org/10.1088/0004-6256/135/6/2446)
- de Pater, I., DeBoer, D., Marley, M., Freedman, R., & Young, R. 2005, *Icarus*, 173, 425, doi: [10.1016/j.icarus.2004.06.019](https://doi.org/10.1016/j.icarus.2004.06.019)
- de Pater, I., Dunn, D., Romani, P., & Zahnle, K. 2001, *Icarus*, 149, 66, doi: [10.1006/icar.2000.6527](https://doi.org/10.1006/icar.2000.6527)
- de Pater, I., & Mitchell, D. L. 1993, *J. Geophys. Res.*, 98, 5471, doi: [10.1029/92JE02810](https://doi.org/10.1029/92JE02810)
- de Pater, I., Sault, R. J., Butler, B., DeBoer, D., & Wong, M. H. 2016, *Science*, 352, 1198, doi: [10.1126/science.aaf2210](https://doi.org/10.1126/science.aaf2210)
- de Pater, I., Wong, M. H., Marcus, P., et al. 2010, *Icarus*, 210, 742, doi: [10.1016/j.icarus.2010.07.027](https://doi.org/10.1016/j.icarus.2010.07.027)
- Edgington, S. G., Atreya, S. K., Trafton, L. M., et al. 1999, *Icarus*, 142, 342, doi: [10.1006/icar.1999.6228](https://doi.org/10.1006/icar.1999.6228)
- Farmer, C. B. 1994, in *IAU Symposium*, Vol. 154, *Infrared Solar Physics*, ed. D. M. Rabin, J. T. Jefferies, & C. Lindsey, 511
- Farmer, C. B., & Norton, R. H. 1989, A high-resolution atlas of the infrared spectrum of the sun and the earth atmosphere from space. A compilation of ATMOS spectra of the region from 650 to 4800 cm⁻¹ (2.3 to 16 μm). Vol. I. The sun.
- Fegley, Jr., B., & Lodders, K. 1994, *Icarus*, 110, 117, doi: [10.1006/icar.1994.1111](https://doi.org/10.1006/icar.1994.1111)
- Féjard, L., Gabard, T., & Champion, J.-P. 2003, *Journal of Molecular Spectroscopy*, 219, 88, doi: [10.1016/S0022-2852\(03\)00019-5](https://doi.org/10.1016/S0022-2852(03)00019-5)
- Flasar, F. M., Kunde, V. G., Abbas, M. M., et al. 2004, *Space Science Reviews*, 115, 169
- Fletcher, L. N., Greathouse, T. K., Orton, G. S., et al. 2016, *Icarus*, 278, 128, doi: [10.1016/j.icarus.2016.06.008](https://doi.org/10.1016/j.icarus.2016.06.008)
- Fletcher, L. N., Orton, G. S., Teanby, N. A., & Irwin, P. G. J. 2009, *Icarus*, 202, 543, doi: [10.1016/j.icarus.2009.03.023](https://doi.org/10.1016/j.icarus.2009.03.023)
- Fletcher, L. N., Orton, G. S., Mousis, O., et al. 2010, *Icarus*, 208, 306, doi: [10.1016/j.icarus.2010.01.005](https://doi.org/10.1016/j.icarus.2010.01.005)
- Friedson, A. J. 2005, *Icarus*, 177, 1, doi: [10.1016/j.icarus.2005.03.004](https://doi.org/10.1016/j.icarus.2005.03.004)

- Gautier, D., Hersant, F., Mousis, O., & Lunine, J. I. 2001, *ApJL*, 550, L227, doi: [10.1086/319648](https://doi.org/10.1086/319648)
- Giles, R. S., Fletcher, L. N., & Irwin, P. G. J. 2017a, *Icarus*, 289, 254, doi: [10.1016/j.icarus.2016.10.023](https://doi.org/10.1016/j.icarus.2016.10.023)
- Giles, R. S., Fletcher, L. N., Irwin, P. G. J., Orton, G. S., & Sinclair, J. A. 2017b, *Geophys. Res. Lett.*, 44, 10, doi: [10.1002/2017GL075221](https://doi.org/10.1002/2017GL075221)
- Griffith, C. A., Bezard, B., Owen, T., & Gautier, D. 1992, *Icarus*, 98, 82, doi: [10.1016/0019-1035\(92\)90209-P](https://doi.org/10.1016/0019-1035(92)90209-P)
- Hanley, T. R., Steffes, P. G., & Karpowicz, B. M. 2009, *Icarus*, 202, 316, doi: [10.1016/j.icarus.2009.02.002](https://doi.org/10.1016/j.icarus.2009.02.002)
- Hersant, F., Gautier, D., & Lunine, J. I. 2004, *Planet. Space Sci.*, 52, 623, doi: [10.1016/j.pss.2003.12.011](https://doi.org/10.1016/j.pss.2003.12.011)
- Howett, C. J. A., Carlson, R. W., Irwin, P. G. J., & Calcutt, S. B. 2007, *Journal of the Optical Society of America B Optical Physics*, 24, 126, doi: [10.1364/JOSAB.24.000126](https://doi.org/10.1364/JOSAB.24.000126)
- Ingersoll, A. P., Adumitroaie, V., Allison, M. D., et al. 2017, *Geophys. Res. Lett.*, 44, 7676, doi: [10.1002/2017GL074277](https://doi.org/10.1002/2017GL074277)
- Irwin, P. G. J., Parrish, P., Fouchet, T., et al. 2004, *Icarus*, 172, 37, doi: [10.1016/j.icarus.2003.09.027](https://doi.org/10.1016/j.icarus.2003.09.027)
- Irwin, P. G. J., Weir, A. L., Taylor, F. W., Calcutt, S. B., & Carlson, R. W. 2001, *Icarus*, 149, 397, doi: [10.1006/icar.2000.6542](https://doi.org/10.1006/icar.2000.6542)
- Irwin, P. G. J., Taylor, F. W., Carlson, R. W., et al. 1999, *Advances in Space Research*, 23, 1623, doi: [10.1016/S0273-1177\(99\)00179-9](https://doi.org/10.1016/S0273-1177(99)00179-9)
- Jacquinet-Husson, N., Scott, N. A., Chedin, A., et al. 2005, *Journal of Quantitative Spectroscopy and Radiative Transfer*, 95, 429
- Janssen, M. A., Hofstadter, M. D., Gulkis, S., et al. 2005, *Icarus*, 173, 447, doi: [10.1016/j.icarus.2004.08.012](https://doi.org/10.1016/j.icarus.2004.08.012)
- Janssen, M. A., Oswald, J. E., Brown, S. T., et al. 2017, *SSRv*, 213, 139, doi: [10.1007/s11214-017-0349-5](https://doi.org/10.1007/s11214-017-0349-5)
- Kalogerakis, K. S., Marschall, J., Oza, A. U., et al. 2008, *Icarus*, 196, 202, doi: [10.1016/j.icarus.2008.03.001](https://doi.org/10.1016/j.icarus.2008.03.001)
- Karalidi, T., Stam, D. M., & Guirado, D. 2013, *A&A*, 555, A127, doi: [10.1051/0004-6361/201321492](https://doi.org/10.1051/0004-6361/201321492)
- Kunde, V. R., & Maguire, W. C. 1974, *Journal of Quantitative Spectroscopy and Radiative Transfer*, 14, 803
- Lellouch, E., Bézard, B., Fouchet, T., et al. 2001, *A&A*, 370, 610, doi: [10.1051/0004-6361:20010259](https://doi.org/10.1051/0004-6361:20010259)
- Lerot, C., Walrand, J., Blanquet, G., Bouanich, J.-P., & Lepère, M. 2003, *Journal of Molecular Spectroscopy*, 219, 329, doi: [10.1016/S0022-2852\(03\)00053-5](https://doi.org/10.1016/S0022-2852(03)00053-5)
- Li, C., Oyafuso, F. A., Brown, S. T., et al. 2017a, *AGU Fall Meeting Abstracts*
- Li, C., Ingersoll, A., Janssen, M., et al. 2017b, *Geophys. Res. Lett.*, 44, 5317, doi: [10.1002/2017GL073159](https://doi.org/10.1002/2017GL073159)
- Loeffler, M. J., Hudson, R. L., Chanover, N. J., & Simon, A. A. 2016, *Icarus*, 271, 265, doi: [10.1016/j.icarus.2016.02.010](https://doi.org/10.1016/j.icarus.2016.02.010)
- Magalhães, J. A., Seiff, A., & Young, R. E. 2002, *Icarus*, 158, 410, doi: [10.1006/icar.2002.6891](https://doi.org/10.1006/icar.2002.6891)
- Malathy Devi, V., Kleiner, I., Sams, R. L., et al. 2014, *Journal of Molecular Spectroscopy*, 298, 11, doi: [10.1016/j.jms.2014.01.013](https://doi.org/10.1016/j.jms.2014.01.013)
- Marcus, P. S. 1993, *ARA&A*, 31, 523, doi: [10.1146/annurev.aa.31.090193.002515](https://doi.org/10.1146/annurev.aa.31.090193.002515)
- Marcus, P. S., Pei, S., Jiang, C.-H., & Hassanzadeh, P. 2013, *Physical Review Letters*, 111, 084501, doi: [10.1103/PhysRevLett.111.084501](https://doi.org/10.1103/PhysRevLett.111.084501)
- Martonchik, J. V., Orton, G. S., & Appleby, J. F. 1984, *ApOpt*, 23, 541, doi: [10.1364/AO.23.000541](https://doi.org/10.1364/AO.23.000541)
- Matcheva, K. I., Conrath, B. J., Gierasch, P. J., & Flasar, F. M. 2005, *Icarus*, 179, 432, doi: [10.1016/j.icarus.2005.06.020](https://doi.org/10.1016/j.icarus.2005.06.020)
- McLean, I. S., Becklin, E. E., Bendiksen, O., et al. 1998, in *Society of Photo-Optical Instrumentation Engineers (SPIE) Conference Series*, Vol. 3354, *Infrared Astronomical Instrumentation*, ed. A. M. Fowler, 566–578
- Millour, E., Forget, F., Spiga, A., et al. 2015, *European Planetary Science Congress*, 10, EPSC2015
- Mishchenko, M., & Travis, L. D. 1998, *JQSRT*, 60, 309, doi: [10.1016/S0022-4073\(98\)00008-9](https://doi.org/10.1016/S0022-4073(98)00008-9)
- Moses, J. I., Fouchet, T., Bézard, B., et al. 2005, *Journal of Geophysical Research (Planets)*, 110, E08001, doi: [10.1029/2005JE002411](https://doi.org/10.1029/2005JE002411)
- Palotai, C., Dowling, T. E., & Fletcher, L. N. 2014, *Icarus*, 232, 141, doi: [10.1016/j.icarus.2014.01.005](https://doi.org/10.1016/j.icarus.2014.01.005)
- Prinn, R. G., & Barshay, S. S. 1977, *Science*, 198, 1031, doi: [10.1126/science.198.4321.1031](https://doi.org/10.1126/science.198.4321.1031)
- Rayner, J., Tokunaga, A., Jaffe, D., et al. 2016, in *Proc. SPIE*, Vol. 9908, *Ground-based and Airborne Instrumentation for Astronomy VI*, 990884
- Read, P. L., Gierasch, P. J., & Conrath, B. J. 2006, *Quarterly Journal of the Royal Meteorological Society*, 132, 1605, doi: [10.1256/qj.05.35](https://doi.org/10.1256/qj.05.35)

- Roos-Serote, M., Atreya, S. K., Wong, M. K., & Drossart, P. 2004, *Planet. Space Sci.*, 52, 397, doi: [10.1016/j.pss.2003.06.007](https://doi.org/10.1016/j.pss.2003.06.007)
- Seiff, A., Kirk, D. B., Knight, T. C. D., et al. 1998, *J. Geophys. Res.*, 103, 22857, doi: [10.1029/98JE01766](https://doi.org/10.1029/98JE01766)
- Showman, A. P., & de Pater, I. 2005, *Icarus*, 174, 192, doi: [10.1016/j.icarus.2004.10.004](https://doi.org/10.1016/j.icarus.2004.10.004)
- Showman, A. P., & Ingersoll, A. P. 1998, *Icarus*, 132, 205, doi: [10.1006/icar.1998.5898](https://doi.org/10.1006/icar.1998.5898)
- Simon, A. A., Wong, M. H., & Orton, G. S. 2015, *ApJ*, 812, 55, doi: [10.1088/0004-637X/812/1/55](https://doi.org/10.1088/0004-637X/812/1/55)
- Simon, A. A., Wong, M. H., Rogers, J. H., et al. 2014, *ApJL*, 797, L31, doi: [10.1088/2041-8205/797/2/L31](https://doi.org/10.1088/2041-8205/797/2/L31)
- Simon-Miller, A. A., Banfield, D., & Gierasch, P. J. 2001, *Icarus*, 154, 459, doi: [10.1006/icar.2001.6742](https://doi.org/10.1006/icar.2001.6742)
- Simon-Miller, A. A., Gierasch, P. J., Beebe, R. F., et al. 2002, *Icarus*, 158, 249, doi: [10.1006/icar.2002.6867](https://doi.org/10.1006/icar.2002.6867)
- Sromovsky, L. A., & Fry, P. M. 2010, *Icarus*, 210, 230, doi: [10.1016/j.icarus.2010.06.039](https://doi.org/10.1016/j.icarus.2010.06.039)
- Tarrago, G., Lacombe, N., Lévy, A., et al. 1992, *Journal of Molecular Spectroscopy*, 154, 30, doi: [10.1016/0022-2852\(92\)90026-K](https://doi.org/10.1016/0022-2852(92)90026-K)
- Tokunaga, A. T., Ridgway, S. T., & Knacke, R. F. 1980, *Icarus*, 44, 93, doi: [10.1016/0019-1035\(80\)90058-5](https://doi.org/10.1016/0019-1035(80)90058-5)
- Venot, O., Hébrard, E., Agúndez, M., et al. 2012, *A&A*, 546, A43, doi: [10.1051/0004-6361/201219310](https://doi.org/10.1051/0004-6361/201219310)
- Visscher, C., & Moses, J. I. 2011, *ApJ*, 738, 72, doi: [10.1088/0004-637X/738/1/72](https://doi.org/10.1088/0004-637X/738/1/72)
- von Zahn, U., Hunten, D. M., & Lehmacher, G. 1998, *J. Geophys. Res.*, 103, 22815, doi: [10.1029/98JE00695](https://doi.org/10.1029/98JE00695)
- Wang, D., Gierasch, P. J., Lunine, J. I., & Mousis, O. 2015, *Icarus*, 250, 154, doi: [10.1016/j.icarus.2014.11.026](https://doi.org/10.1016/j.icarus.2014.11.026)
- Wang, D., Lunine, J. I., & Mousis, O. 2016, *Icarus*, 276, 21, doi: [10.1016/j.icarus.2016.04.027](https://doi.org/10.1016/j.icarus.2016.04.027)
- Weidenschilling, S. J., & Lewis, J. S. 1973, *Icarus*, 20, 465, doi: [10.1016/0019-1035\(73\)90019-5](https://doi.org/10.1016/0019-1035(73)90019-5)
- Wong, M. H. 2009, *Icarus*, 199, 231, doi: [10.1016/j.icarus.2008.08.017](https://doi.org/10.1016/j.icarus.2008.08.017)
- Wong, M. H., Atreya, S. K., Kuhn, W. R., Romani, P. N., & Mihalka, K. M. 2015, *Icarus*, 245, 273, doi: [10.1016/j.icarus.2014.09.042](https://doi.org/10.1016/j.icarus.2014.09.042)
- Wong, M. H., de Pater, I., Asay-Davis, X., Marcus, P. S., & Go, C. Y. 2011, *Icarus*, 215, 211, doi: [10.1016/j.icarus.2011.06.032](https://doi.org/10.1016/j.icarus.2011.06.032)
- Wong, M. H., Lunine, J., Atreya, S. K., et al. 2008, in *Oxygen in the Solar System, Reviews in Mineralogy and Geochemistry*, ed. MacPherson, G. J., Mittlefehldt, D. W., Jones, J. & Simon, S. B., Vol. 68, 219–246
- Wong, M. H., Mahaffy, P. R., Atreya, S. K., Niemann, H. B., & Owen, T. C. 2004, *Icarus*, 171, 153, doi: [10.1016/j.icarus.2004.04.010](https://doi.org/10.1016/j.icarus.2004.04.010)